REVIEW

Advances in van der Waals thermoelectric materials: prospects and challenges

Marco Fronzi, [iD] *a Paolo Mele, [iD] b Amanda V. Ellis [iD] c and Catherine Stampfl [iD] a

This paper provides a comprehensive review of models and advancements in the discovery of novel van der Waals (vdW) layered materials for thermoelectric applications. The theoretical complexities involved in predicting thermoelectric properties are explored, highlighting the key aspects and challenges in the accurate prediction of fundamental thermoelectric parameters. First-principles and semiclassical models are illustrated, and their respective strengths and limitations in guiding experimental efforts are discussed. The synthesis methods are discussed, suggesting the strengths and limitations of each approach. Current state-of-the-art characterisation techniques for measuring key thermoelectric properties are reported, along with examples of top-performing vdW materials. Critical challenges in developing high-efficiency thermoelectric materials are mentioned, suggesting future research directions.

a School of Physics, The University of Sydney, Australia.
E-mail: marco.fronzi@sydney.edu.au
b College of Engineering, Shibaura Institute of Technology, 307 Fukasaku, Minuma-ku, Saitama 337-8570, Japan
c School of Chemical Engineering, University of Melbourne, Australia

I. Introduction

Thermoelectric transformation is a versatile form of energy conversion that efficiently uses the abundant waste heat generated by current industrial processes. This technology is

Marco Fronzi

Marco Fronzi is a Senior Research Scientist at the School of Physics, University of Sydney, specialising in computational condensed matter physics. He received his PhD from the University of Rome "Tor Vergata". After his PhD, he was later awarded a Japan Society for the Promotion of Science Fellowship, and he has held research appointments in Japan, Ireland, China and Australia. His scientific interests focus on the application of quantum mechanical, semi-classical and machine learning models to understand and predict the properties of novel materials with technological relevance. His work explores materials for energy conversion applications, including thermoelectric, solar-to-chemical processes, photovoltaics and other energy conversion processes.

Paolo Mele

Prof. Paolo Mele is currently a tenured Professor at Shibaura Institute of Technology (Omiya campus, Saitama, Japan). He obtained a Masters degree in Chemistry and a PhD in Chemical Sciences from the University of Genoa (Italy). In 2003, he moved to ISTEC-SRL in Tokyo to study melt-textured ceramic superconductors. He then worked as a postdoc at Kyoto University (JSPS fellowship) from 2004 to 2007, Kyushu Institute of Technology (JST fellowship) from 2007 to 2011, Hiroshima University (as lecturer) from 2011 to 2014, and Muroran Institute of Technology (as Associate Professor) from 2015 to 2018, before reaching his current position. His research interests include materials for energy and sustainable development (superconductors and thermoelectrics); fabrication and characterization of thin films of oxides, ceramics, and metals; study of the effect of nanostructuration on physical properties; thermal transport; vortex matter and the development of new materials for photoelectrocatalysis. Recently, Prof. Mele has focused on the intersection of materials science and computational methods, with a particular emphasis on sustainable energy materials.

not only advantageous for converting heat into electricity, enabling the recovery of energy that would otherwise be lost through the Seebeck effect, but it is also effective in reverse using electricity to drive cooling processes through the Peltier effect.[1,2] These dual capabilities make thermoelectric materials highly valuable for both power generation and cooling applications, offering a sustainable solution to enhance energy efficiency and reduce overall energy consumption in various industries.

Recently, the integration of thermoelectric materials in emerging technological areas has been reported. Of particular interest, thermoelectric materials are starting to find their way into artificial intelligence (AI) to implement functionalities such as hand motion recognition[3] and robotic hand response.[4] Further, they are used in fire alarming systems[5] and smart building technologies[6] where the conversion of thermal fluctuations into usable electrical signals improves automation and energy efficiency. These materials especially in the 2D van der Waals (vdW) systems have shown rather specific transport characteristics which make them very promising for future electronic and optoelectronic devices.

The thermoelectric conversion efficiency is quantified by the figure of merit, $zT = \dfrac{S^2 \sigma T}{\kappa}$ and the power factor PF = $S^2\sigma$. In this expressions z is a dimensionless coefficient that reflects the material's performance, whereas S is the Seebeck coefficient, which quantifies the voltage generated in response to a temperature difference, σ is the electrical conductivity, T is the absolute temperature, and κ is the thermal conductivity.[7] High zT values indicate high efficiency in thermal-to-electrical energy conversion, whereas the power factor (PF) quantifies the ability of a material to generate electrical power from a given temperature gradient.[8]

Van der Waals (vdW) layered materials have emerged as a promising class of thermoelectric materials.[9] Their key feature consists in the low dimensionality of the chemical bonds along the x–y plane, held together by weak van der Waals forces along the perpendicular direction, allowing for easy mechanical exfoliation and the creation of atomically thin layers that can be combined as Lego blocks, offering a huge space of unexplored novel materials with exotic chemical and physical properties.[10]

The reduced dimensionality and consequent electronic wave-function confinement make this class of materials fundamentally different from their three-dimensional counterparts. Proper engineering of the layers can significantly enhance carrier mobility and reduce lattice thermal conductivity, leading to an increased thermoelectric figure of merit and overall conversion efficiency. These effects on key parameters are driven by quantum confinement, and highlight the potential for optimising thermoelectric properties in two-dimensional materials.[11,12]

Compared to bulk materials, the quantum confinement and reduced dimensionality in 2D systems can enhance the density of states near the Fermi level, leading to an improved Seebeck coefficient, while phonon scattering at the atomic scale can reduce thermal conductivity, thereby increasing the overall thermoelectric efficiency.

Recent advancements in the synthesis and characterisation of vdW layered materials have opened new avenues for optimising their thermoelectric performance.[13] Various methods such as mechanical exfoliation, chemical vapour deposition (CVD), and solution-based techniques have been employed to produce high-quality vdW layers with controlled thickness and composition.[10,14,15] Each method offers distinct advantages and challenges in terms of

Professor Ellis is the Head of the School of Chemical and Biomedical Engineering at The University of Melbourne, Australia. She graduated from the University of Technology, Sydney in 2003 and has undertaken postdoctoral appointments at Rensselaer Polytechnic Institute, New Mexico State University and Callaghan Innovations, NZ. She has been a Professor and Australian Research Future Fellow at Flinders University, South Australia. Her work focuses on interfacial engineering and chemistries of materials for energy storage/harvesting and device application.

Amanda V. Ellis

Catherine Stampfl is a Professor in the School of Physics at The University of Sydney working in the area of computational condensed matter physics. She received her PhD from La Trobe University, Australia, and Habilitation from the Technical University, Berlin, Germany. She has worked at the Fritz-Haber-Institute of the Max-Planck Society, Berlin, in the Electronic Materials Laboratory at Xerox Palo Alto Research Center, California, in the Department of Physics and Astronomy, Northwestern University, Evanston Chicago. She has published over 300 papers and is a Fellow of the Australian Academy of Science and the Royal Society of New South Wales.

Catherine Stampfl

scalability, uniformity, and material quality. For instance, CVD can produce large-area monolayers suitable for practical applications, while solution-based methods offer a scalable route for mass production.[16,17]

Several layered 2D materials have been experimentally investigated for their thermoelectric performance, with maximised power factors achieved under specific conditions. The key categories of high-performing thermoelectric 2D materials include: transition metal dichalcogenides (TMDs), such as MoS_2 and WSe_2, which have shown promising results when carrier concentration is tuned through electric double-layer gating; titanium disulphide (TiS_2), which exhibits moderate thermoelectric performance when intercalated with organic molecules due to enhanced charge transport; graphene, which, despite its intrinsically low Seebeck coefficient, achieves an exceptional power factor when placed on hexagonal boron nitride (h-BN), benefiting from reduced carrier scattering; and black phosphorus (bP), known for its anisotropic electronic properties, which demonstrates enhanced thermoelectric performance under electrostatic gating.

Table 1 summarises the main categories of layered 2D materials together with the notable features. These findings highlight the tunability of thermoelectric properties in 2D systems and underscore their potential for energy harvesting applications.

Despite these advancements, several challenges remain, and achieving high zT values requires a delicate balance between electrical conductivity and thermal conductivity.[18] Increasing electrical conductivity often leads to an increase in thermal conductivity, which can be detrimental to thermoelectric performance.[8] Therefore, strategies to decouple these properties are critical, and the contribution of defects, grain boundaries, and layer-to-layer interactions plays a significant role.[19] Additionally, the integration into functioning devices while maintaining their intrinsic properties is a challenge that needs to be addressed.[20]

This paper reviews the recent advancements in vdW layered thermoelectric materials, identifies the challenges faced in their development, and explores potential future research directions. We discuss various synthesis methods, the structural and electronic properties of these materials, and their thermoelectric performance. We also highlight recent experimental and theoretical frameworks that have contributed to our understanding of the fundamental

mechanisms. By addressing the current challenges and exploring innovative solutions, we aim to provide insights into the future directions of research.

II. vdW layered structures as good thermoelectric materials

Achieving high thermoelectric performance requires optimising several interrelated parameters: the Seebeck coefficient (S), electrical conductivity (σ), and thermal conductivity (κ). The figure of merit, $zT = \frac{S^2 \sigma T}{\kappa}$, combines these parameters into a single value that measures overall device efficiency. Increasing S can improve the voltage generated from a temperature gradient, but it often comes at the cost of reducing σ. Similarly, while reducing κ improves heat retention, it can be challenging because increasing σ often leads to a proportional increase in κ. The key to designing high-performance thermoelectric devices is to decouple these parameters, for instance by engineering materials with low lattice thermal conductivity but high electrical conductivity, such as vdW materials. By carefully balancing these parameters, researchers can design materials that perform optimally under real-world conditions. This requires not only an understanding of the material's intrinsic properties but also how these properties translate to device performance in practical applications.

The formulation of these quantities can be expressed as a function of the fundamental physical parameters. The Seebeck coefficient is:

$$S = -\frac{\pi^2 k_B{}^2 T}{2e E_F(V, \varepsilon, f, g(\varepsilon, V), \mu)}, \quad (1)$$

where k_B is the Boltzmann constant, T is the absolute temperature, e is the elementary charge, and E_F is the Fermi energy which is a function of the potential V, the energy level ε, the Fermi–Dirac distribution function f, the density of states $g(\varepsilon, V)$, and the chemical potential μ.

$$\sigma = \frac{q^2 C_e D_e}{k_B T}, \quad (2)$$

where q is the elementary charge, D_e is the electron diffusion coefficient, and C_e is the electron concentration.

Thermal conductivity, with contribution from electron and phonon diffusion ($\kappa = \kappa_e + \kappa_p$), has the general form:

Table 1 Thermoelectric properties of main 2D vdW material families

Material family	Notable features
Transition metal dichalcogenides (TMDs)	Tunable electronic properties, ranging from semiconducting to metallic behaviours
Group IV–VI compounds	Anisotropic crystal structures with high Seebeck coefficients and low thermal conductivity
Janus monolayers	Structural asymmetry leads to anisotropic electronic and vibrational properties, resulting in high thermoelectric performance
MXenes	Surface functionalization can induce semiconducting properties with good thermoelectric performance

$$\kappa_{e,p} = \frac{n \langle v \rangle \lambda c_V}{3 N_A}. \tag{3}$$

Here n is the number of particles per unit volume, $\langle v \rangle$ is the mean particle speed, λ is the mean free path, c_V is molar heat capacity and N_A is Avogadro's number.

A low lattice thermal conductivity, high electric conductivity and large Seebeck coefficient are desired to maintain a high zT. The complex inter-correlations between the variables in the definition of each thermoelectric
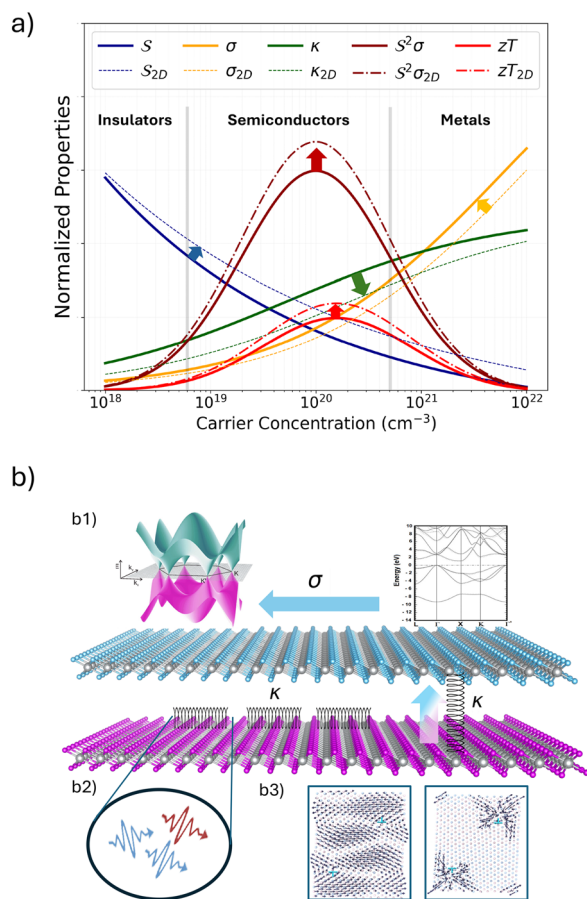

Fig. 1 a) Schematic trend of normalised properties as a function of carrier concentration for both 3D and 2D materials. The plot shows the behaviour of the Seebeck coefficient (S), electrical conductivity (σ), thermal conductivity (κ), power factor ($S^2\sigma$), and figure of merit (zT) for carrier concentrations ranging from 10^{18} to 10^{22} cm^{-3}. Solid lines represent 3D material properties: S (dark blue), σ (orange), κ (dark green), $S^2\sigma$ (dark red), and zT (red). Dashed and dotted lines represent corresponding 2D material properties: S_{2D} (dark blue, dashed), σ_{2D} (orange, dashed), κ_{2D} (dark green, dashed), $S^2\sigma_{2D}$ (dark red, dash-dotted), and zT_{2D} (red, dash-dotted). The x-axis is logarithmically scaled to show the wide range of carrier concentrations, and the y-axis displays normalised properties with a limit up to 2.5. The legend at the top center provides a clear distinction between 3D and 2D properties for each parameter. b1) Schematic representation of the 2D structural and electronic features that potentially contribute to the shift of the variables in the plot a). Here, b2) represents the two dimensional phonon–phonon scattering, b3) localised phonon modes, as extracted from the work of Sun *et al.*[21]

parameter make it difficult to improve all the properties simultaneously.

In general, 2D materials can leverage their low dimensionality to address some of the challenges that make it difficult to simultaneously adjust all variables to a desired target (as schematically illustrated in Fig. 1). The potential benefit can be summarised here:

1. 2D quantum confinement leads to a sharper density of states ($g(\varepsilon,V)$) near the Fermi level, which increases the energy dependence of the electronic states, thus increasing S.[11,22] Firstly, the improvement in the Seebeck coefficient in superlattices is generated from the step-like $n(\varepsilon,V)$, produced by $n(\varepsilon,V) = g(\varepsilon,V)f$, where $g(\varepsilon,V)$ is the density of states (DOS) per unit volume and per unit energy. This $g(\varepsilon,V)$ can be increased through carrier-pocket engineering in superlattices. When the width of the barrier layer is comparable to that of the quantum well, the localised electron wave function will be released. The anisotropy of the band structure offers a possibility of tuning the relative contributions of different carrier pockets at the Fermi surface by changing the superlattice parameters, such as the growth direction, lattice period, and layer thickness. This leads to a sharp shift in the local DOS and an increment of the Seebeck coefficient with little change in the carrier concentration, thus decoupling the electrical conductivity and the Seebeck coefficient. In doped layers, the presence of ionised impurity scattering centers confined in the potential well and blocked by the potential barrier reduces the carrier scattering events, resulting in higher carrier mobility, which has a slight influence also on phonon transport, leading to μ/κ_p values of a superlattice being much higher than those of bulk materials.

2. Interface effects can be divided into three categories: specular, diffuse, and hybrid (partially specular and partially diffuse). At a diffuse interface, the thermal conductivity along the layers is irrelevant to the transmissivity and reflectivity. Therefore, the thermophysical properties are decoupled and can be calculated from the individual layers separately.[22]

3. In the presence of delocalised graphene-like π-electrons, high electrical conductivity can be achieved. Furthermore, the 2D structure reduces scattering events, which increases charge carrier mobility.[23] The heat carried by charges during transmission links electrical and electronic thermal conductivity through the Wiedemann–Franz law. Although electric and electronic thermal conductivity are distinct properties, they exhibit similar behaviour at a specific temperature, and essentially the ratio of these conductivities can be approximated to the Lorentz number.[24]

4. The weak interlayer vdW forces will result in low phonon transport across layers, significantly reducing lattice thermal conductivity.[19,25] The phonon mean free path (MFP) is substantially different when comparing 2D and three-dimensional (3D) materials: in 2D materials, phonons are confined to two dimensions, which generally leads to different scattering mechanisms compared to 3D materials.[26,27] Phonon–phonon scattering and boundary

scattering tend to be more significant in 2D materials because of the increased surface-to-volume ratio. As a general trend, the reduced dimensionality in 2D materials like graphene or transition metal dichalcogenides can lead to longer phonon mean free paths, due to the fewer available scattering channels compared to 3D materials[28] In 3D materials, phonons have more available scattering channels due to the higher number of degrees of freedom. This typically results in shorter phonon mean free paths compared to 2D materials.[29] Furthermore, 2D superlattices can reduce thermal conductivity upon creation of phonon band gaps and flattened phonon dispersion relations, which limit the group velocity of phonons and enhance scattering, leading to lower thermal transport.[30] However, phonon scattering depends on the nature of the specific interface that can be appropriately engineered, and phonon transmission can be either facilitated or hindered. Proper engineering of the interface and the presence of defects, grain boundaries, and interfaces in 2D heterostructures may increase phonon scattering, which disrupts the flow of heat-carrying phonons and reduces thermal conductivity. Furthermore, phonon modes can become localised, which effectively limits thermal conductivity as it reduces the overall phonon transmission across the material.[21]

5. The quantum-confinement produces a new kind of Umklapp scattering process. The finite layer thickness and the large superlattice constant lead to a small Brillouin zone in the stacking direction. The Umklapp process is confined in this small Brillouin zone, which reduced thermal conductivity. The effect also impacts the thermal conductivity along the layers.

III. Theoretical complexity in thermoelectric properties calculations

The calculation of thermoelectric parameters requires a detailed understanding of the electronic structure and phonon dynamics within a material.[31,32] The Seebeck coefficient, for instance, is a function of the electron density and the transport distribution function, both of which are sensitive to the material's band structure and scattering mechanisms. Similarly, electrical conductivity is governed by the charge carriers' mobility and concentration, which are significantly affected by impurities, defects, and temperature. Thermal conductivity, particularly the lattice contribution, involves complex phonon scattering processes that are difficult to model accurately due to the intricate interactions between phonons, defects, and impurities within the crystal lattice.

Within a quantum mechanics framework, the Seebeck coefficient can be reformulated as follows:

$$S = \frac{L_{12}}{eTL_{11}} \quad (4)$$

where L_{11} and L_{11} are the transport coefficient related to current–energy and current–current correlations, respectively.

The electrical conductivity in the $(\sigma_{\alpha\beta})$ directions is given by:

$$\sigma_{\alpha\beta} = \frac{\hbar}{V} \sum_{\mathbf{k}} \text{Tr}\left[\hat{J}_{\alpha} \hat{G}^R(\mathbf{k}, \varepsilon) \hat{J}_{\beta} \hat{G}^A(\mathbf{k}, \varepsilon) \right]. \quad (5)$$

Here, $\hbar$ is the reduced Planck constant, V is the volume of the system, $\mathbf{k}$ is the wavevector, indicating the momentum state of an electron, $\hat{J}_{\alpha}$, $\hat{J}_{\beta}$ are the current operators in the α and β directions, and $\hat{G}^R(\mathbf{k}, \varepsilon)$, $\hat{G}^A(\mathbf{k}, \varepsilon)$ are the retarded and advanced Green's functions, describing the propagation of electronic states and ε is the energy of the electronic states.

The electronic contribution to the thermal conductivity (κ_e) is:

$$\kappa_e = \frac{1}{T}\left(\frac{L_{22}}{e^2} - \frac{L_{12}^2}{e^2 L_{11}} \right), \quad (6)$$

where L_{22}, L_{12} and L_{11} are the transport coefficient related to energy–energy, current–energy and current–current correlations, respectively.

The phonon thermal conductivity (κ_p) is given by:

$$\kappa_p = \frac{1}{V}\int_0^{\infty} \mathrm{d}t \langle \hat{J}_Q(t)\hat{J}_Q(0)\rangle, \quad (7)$$

where V is the volume of the system, t is the time, $\hat{J}_Q(t)$ is the heat current operator at time t, and $\langle \hat{J}_Q(t)\hat{J}_Q(0)\rangle$ is the correlation function of the heat current, describing how the heat current at time t is related to that at time 0.

The evaluation of the Seebeck coefficient, electrical conductivity, and thermal conductivities purely from first-principles calculations is challenging due to the complex nature of electron and phonon interactions. These calculations require accurate modelling of quantum states, many-body interactions, and non-equilibrium conditions, all of which are computationally intensive. Additionally, accurately accounting for temperature dependence and scattering processes adds further complexity. The quantum mechanical treatment of these quantities often involves advanced methods such as Greens functions and the Kubo formula, making the computations both resource-intensive and technically demanding.

A. Calculation approaches

Quantum mechanical methods, such as density functional theory (DFT), can provide accurate descriptions of the electronic and phonon structure and the behaviour of atomic systems at 0 K. The choice of the suitable exchange-correlation functional, which may significantly impact the energetics and geometry of the materials, can be complemented by a semi-empirical approach. Among the functionals, the local density approximation (LDA) is computationally efficient and works well for systems with slowly varying electron densities, such as simple metals and semiconductors.[33,34] However, it tends to over-bind in 2D materials, leading to inaccurate interlayer distances and poor modelling of van der Waals (vdW) interactions, which are

crucial for layered materials like graphene and transition metal dichalcogenides (TMDCs). The generalised gradient approximation (GGA) improves upon the LDA by considering the gradient of the electron density, offering better predictions for a wider range of materials, including molecules, surfaces, and bulk systems.[35] The GGA, particularly the PBE functional, is widely used due to its balance between accuracy and computational cost. However, the GGA still underestimates binding energies and overestimates bond lengths in weakly bound systems, leading to possibly large inaccuracies in vdW materials. It also struggles with systems exhibiting strong electron correlation, such as certain TMDCs and complex oxides.[35] Meta-GGA functionals, like strongly constrained and appropriately normed (SCAN), capture the delicate balance between covalent and vdW interactions, leading to more accurate modelling of these systems. However, the inclusion of higher-order terms in meta-GGA functionals increases computational complexity, making them more resource-intensive and potentially less consistent across different material types.[36] Finally, hybrid functionals, such as B3LYP and HSE06, combine exact Hartree–Fock exchange with GGA or LDA, resulting in the highest accuracy for electronic properties, especially for 2D vdW materials.[37] These functionals are effective for calculating accurate band gaps and other electronic properties in semiconductors, insulators, and systems with significant electron correlation. However, hybrid functionals are computationally demanding and their accuracy can be sensitive to the choice of parameters, such as the fraction of Hartree–Fock exchange, which may need to be tailored for specific systems.

Additionally, van der Waals functionals must be included in DFT calculations due to the inability of DFT to capture dispersion interactions or long-range correlation effects, which is crucial in 2D materials. These functionals provide a way to incorporate non-local correlations and model weak interlayer interactions.[38,39] Recent advancements have reduced the computational cost of vdW functionals, making them more comparable to traditional GGA functionals. This has allowed for their application in larger and more complex systems without significant computational penalties.[40] A common issue with vdW functionals is their tendency to either overestimate or underestimate interaction strengths. For example, the original vdW-DF may overestimate long-range forces, while vdW-DF2 might underestimate key coefficients like the C_6 term, affecting the accuracy of dispersion energy predictions.[38,39] The performance of vdW functionals is closely tied to the choice of exchange functional. For instance, using revPBE in vdW-DF can result in inaccurate binding distances. Alternative exchange functionals, such as optB88, have been developed to improve accuracy, but the optimal choice is still strongly system dependent, and there is currently no vdW functional that performs consistently across different materials.[38,39]

Although the DFT models provide a detailed understanding of electronic structure, calculating thermoelectric parameters requires an additional theoretical framework to describe and quantify transport mechanisms.

The Boltzmann transport equation (BTE) is a common model used to approximate the theoretical value of these properties, within a semi-classical framework.[41,42] Solving the BTE requires detailed knowledge of the relaxation times, which are influenced by various scattering mechanisms, including phonon–phonon, electron–phonon, and impurity scattering. Accurately determining these relaxation times often necessitates sophisticated computational techniques, such as *ab initio* molecular dynamics simulations, which can be computationally expensive and complex.[43–45] Moreover, the interplay between electronic and thermal transport properties adds another layer of complexity.[46] For instance, strategies to reduce thermal conductivity, such as introducing nano-structures or alloying, can adversely affect the electrical conductivity and the Seebeck coefficient. This interdependence means that theoretical models must simultaneously account for multiple transport phenomena and their interactions, making accurate predictions particularly challenging. For example, the phonon BTE describes thermal transport in a solid where phonons govern the process through vibrations of the crystal's atoms, and any alteration in these vibrations can significantly impact the thermal and electrical transport properties.[47,48] Additionally, the relaxation time approximation simplifies the BTE by assuming that all scattering processes can be characterised by a single relaxation time, which is not always valid. This approximation is often used in conjunction with the Wigner–Boltzmann transport equation for systems with homogeneously distributed defects and under the assumption of a linear response to external electric fields.[49,50]

Within the semi-classical BTE approximations, the formulation of the Seebeck coefficient can be redefined as:[51–53]

$$S = -\frac{1}{eT}\frac{\int \tau(\varepsilon) v^2(\varepsilon)(\varepsilon-\mu)\left(-\frac{\partial f(\varepsilon)}{\partial \varepsilon}\right)g(\varepsilon)\,\mathrm{d}\varepsilon}{\int \tau(\varepsilon) v^2(\varepsilon)\left(-\frac{\partial f(\varepsilon)}{\partial \varepsilon}\right)g(\varepsilon)\,\mathrm{d}\varepsilon}, \tag{8}$$

where e is the elementary charge, T is the absolute temperature, ε is the energy of the charge carriers, μ is the chemical potential (Fermi level), v is the electron group velocity, f is the Fermi–Dirac distribution function, and τ is the relaxation time,

The integration over all possible energy states, accounting for the distribution of carriers and their energy-dependent transport properties, which are influenced by the material's electronic structure and various scattering mechanisms, makes the calculation of S relatively complex.

The electron conductivity is then given by:

$$\sigma = e^2 \int \tau(\varepsilon) v^2(\varepsilon)\left(-\frac{\partial f(\varepsilon)}{\partial \varepsilon}\right)g(\varepsilon)\,\mathrm{d}\varepsilon. \tag{9}$$

The integral requires precise knowledge of the energy-dependent transport distribution function and how the

© 2025 The Author(s). Published by the Royal Society of Chemistry

RSC Appl. Interfaces, 2025, **2**, 852–872 | 857

carrier distribution changes with energy, making it necessary to consider detailed interactions within the material.

The thermal conductivity in the context of electronic contributions (often denoted as κ_e) can be expressed quantum mechanically as:

$$\kappa_e = \frac{1}{T}\left[\int \tau(\varepsilon)v^2(\varepsilon)(\varepsilon-\mu)^2\left(-\frac{\partial f(\varepsilon)}{\partial \varepsilon}\right)g(\varepsilon)\mathrm{d}\varepsilon\right] - \sigma S^2 T. \quad (10)$$

This expression is complex because it involves two integrals, one of which is included in $\sigma S^2 T$, that account for the energy distribution of carriers and their transport properties. In particular, the second term ($\sigma S^2 T$) accounts for the correlation between energy levels, adding further complexity to the calculations. An example of calculated S, σ and power factor (PF) within the BTE model is shown in Fig. 2.

The Landauer transport equations (LTE) provide an alternative model to understand electronic transport, particularly at the nanoscale. Unlike the BTE, Landauer theory models conductance as a quantum mechanical transmission problem.[55–57] It assumes ballistic transport, where electrons traverse the material without scattering, making it ideal for analysing transport in mesoscopic systems like quantum dots and nanowires.[58] While the BTE excels in describing diffusive transport where scattering is significant, Landauer theory gives a more accurate description in systems where quantum coherence is maintained over the length of the conductor. The Landauer approach is particularly useful in systems where quantum effects are non-negligible and where ballistic transport dominates, like low dimensional materials, offering a powerful alternative to the semi-classical nature of the BTE.[59]

Within the Landauer model the Seebeck coefficient, electron conductivity and electronic thermal conductivity become:[51,60]

$$S = -\frac{1}{eT}\frac{\int T_e(\varepsilon)(\varepsilon-\mu)\left(-\frac{\partial f(\varepsilon)}{\partial \varepsilon}\right)\mathrm{d}\varepsilon}{\int T_e(\varepsilon)\left(-\frac{\partial f(\varepsilon)}{\partial \varepsilon}\right)\mathrm{d}\varepsilon}, \quad (11)$$

$$\sigma = e^2\frac{2}{h}\int_{-\infty}^{\infty} T(E)\left(-\frac{\partial f(E)}{\partial E}\right)\mathrm{d}E, \quad (12)$$

$$\kappa_e = \frac{2}{hT}\left[\int T_e(\varepsilon)(\varepsilon-\mu)^2\left(-\frac{\partial f(\varepsilon)}{\partial \varepsilon}\right)\mathrm{d}\varepsilon\right] - \sigma S^2 T, \quad (13)$$

where $T_e(\varepsilon)$ is the electron transmission function.

The Landauer formalism focuses on quantum mechanical aspects, particularly the transmission function that reflects the probability of carriers traversing a conductor. It is best suited for mesoscopic systems where phase coherence is crucial, whereas Boltzmann approximation relies on

Fig. 3 Electronic transmission, Seebeck coefficient, power factor, and thermoelectric figure of merit are plotted around the Fermi level for a) 2H-ZrSe$_2$, b) 2H-ZrTe$_2$, c) 2H-HfS$_2$, and d) 2H-HfSe$_2$ using the LTE model.[61]
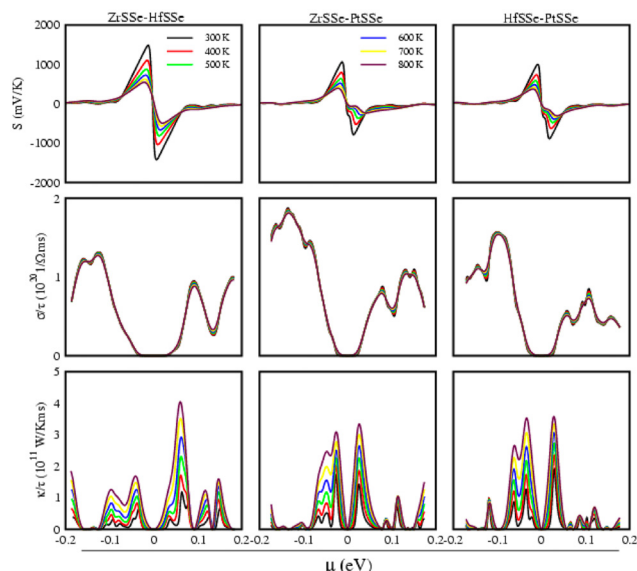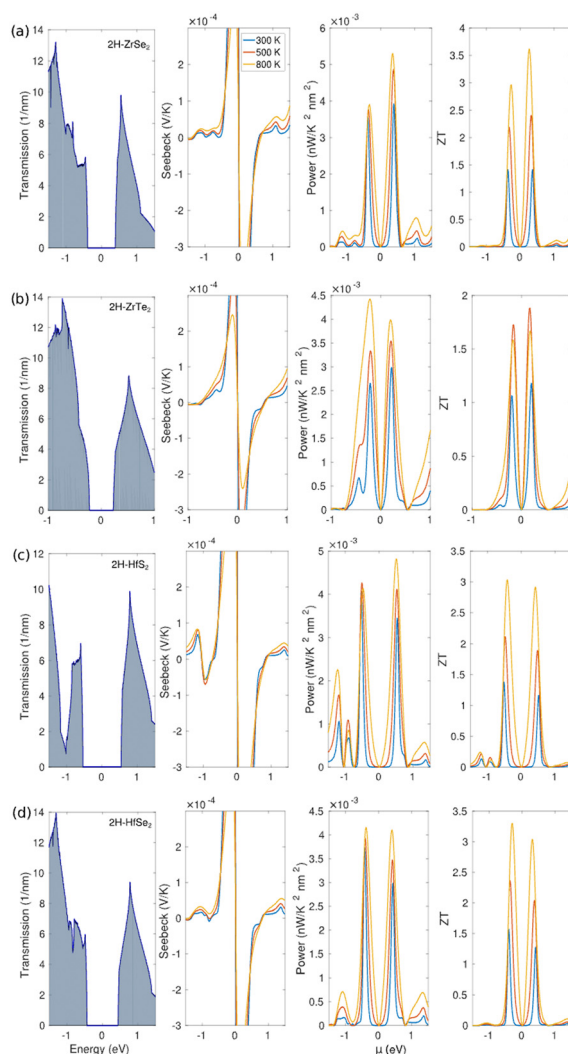

Fig. 2 Seebeck coefficient (first row), electrical conductivity (second row) and power factor (third row) of selected vdW heterostructures under strain, calculated within the BTE model by Ahmad *et al.*[54]

semiclassical assumptions, with a focus on scattering events, relaxation times, and velocities of carriers. It is more applicable to bulk materials where quantum coherence is not significant. Examples of the calculated electronic transmission, Seebeck coefficient, power factor, and thermoelectric figure of merit are shown in Fig. 3.

Both approaches are essential for comprehensively understanding transport phenomena, with Landauer theory providing a more straightforward, albeit idealised, perspective compared to the more complex, scattering-based BTE.[62]

To evaluate the main contribution to thermal conductivity in semiconductors and insulators it is essential to analyse the underlying phonon dynamics, which still involves solving the transport equations, and can be approached using methods like the discrete ordinates method or spherical harmonics expansions. All these methods aim to solve the transport equations numerically, considering anisotropic relaxation times and accounting for phonon–phonon interactions.[63–67] The phonon thermal conductivity quantified using lattice dynamics calculations is given by:

$$\kappa_{\mathrm{p}} = \frac{1}{NV_{\mathrm{c}}} \sum_{\lambda} C_{\lambda} \mathbf{v}_{\lambda} \otimes \mathbf{v}_{\lambda} \tau_{\lambda}^{\mathrm{SMRT}}, \tag{14}$$

where $\tau_{\lambda}^{\mathrm{SMRT}}$ is the single-mode relaxation time (SMRT), and C_{λ} is the mode heat capacity defined as

$$C_{\lambda} = k_{\mathrm{B}} \left(\frac{\hbar\omega_{\lambda}}{k_{\mathrm{B}}T}\right)^2 \frac{\exp(\hbar\omega_{\lambda}/k_{\mathrm{B}}T)}{[\exp(\hbar\omega_{\lambda}/k_{\mathrm{B}}T) - 1]^2}. \tag{15}$$

Here, N is the number of unit cells, V_{c} the volume of the unit cell, C_{λ} the mode heat capacity, $\mathbf{v}_{\lambda}$ the phonon group velocity, $\tau_{\lambda}^{\mathrm{SMRT}}$ the single-mode relaxation time, $\hbar$ the reduced Planck's constant, ω_{λ} the phonon frequency, and $n_{\lambda}(T)$ the Bose–Einstein distribution function. Complexity arises from the need to integrate over all phonon frequencies and account for the frequency-dependent specific heat, phonon group velocity, and mean free path, which all depend on the intricate details of the lattice dynamics.

In nano-structures and low dimensional systems like quantum wells and superlattices, electron–phonon interactions can lead to non-equilibrium phonon distributions, and should be included for an accurate analysis.[68–71]

IV. Synthesis methods

Although the experimental measurement of thermoelectric properties requires well-established techniques, the fabrication of 2-dimensional vdW materials requires particular expertise due to the relative novelty of their synthesis and handling methods. The synthesis of 2D layered materials is typically achieved by employing mechanical exfoliation, chemical vapour deposition (CVD), and solution-based techniques.

Mechanical exfoliation, also known as the "scotch tape" method, while effective for producing high-quality monolayers, faces challenges in scalability.[10] Innovations in

automated mechanical exfoliation systems have improved throughput and consistency, making the technique more practical for research applications.[23] Detailed steps of this method are discussed in the following section.

CVD has emerged as a key technique for synthesising large-area, high-quality monolayers and heterostructures with precise control over layer thickness and composition. For example, CVD-grown monolayer MoS_2 using sulphur and molybdenum hexacarbonyl precursors demonstrates high uniformity and excellent electronic properties, making it suitable for various electronic and optoelectronic applications.[14] Additionally, the CVD synthesis of large-area graphene and transition metal dichalcogenides (TMDs) has facilitated the development of high-performance transistors and photodetectors.[16]

Solution-based methods, including liquid-phase exfoliation and chemical synthesis, offer scalable routes for producing large quantities of vdW materials. These methods involve dispersing bulk crystals in solvents followed by exfoliation through sonication or chemical reactions. The scalability and simplicity of solution-based methods make them attractive for industrial applications, despite challenges in achieving uniformity and controlling defects.[15]

A. Mechanical exfoliation

The mechanical exfoliation process has been a pioneering technique for isolating monolayers from bulk vdW layered materials. This method involves peeling layers from a bulk crystal using adhesive tape, which are then transferred onto a substrate. Its simplicity and effectiveness in producing high-quality monolayers made it popular in early studies of graphene and other 2D materials.[10] However, despite its success in research applications, mechanical exfoliation faces significant limitations in scalability and reproducibility.

The process of mechanical exfoliation typically involves several steps:

1. Preparation of bulk crystal: a bulk vdW crystal is cleaved to expose a fresh surface. This initial step is crucial as it ensures that the layers to be exfoliated are clean and free from contaminants, which can otherwise affect the quality of the exfoliated layers.[10,23]

2. Adhesive application: adhesive tape is applied to the cleaved surface and then peeled away, capturing thin layers of the material. This method has been successfully used to exfoliate a variety of vdW materials, including graphene, MoS_2, and other transition metal dichalcogenides (TMDs).[72,73]

3. Transfer to substrate: the tape with exfoliated layers is pressed onto a substrate, such as silicon dioxide (SiO_2) on silicon (Si), and then carefully removed to leave behind the 2D layers. This transfer step is critical to achieving well-aligned and defect-free monolayers.[74]

Several advancements have been made to refine this technique. For instance, using micro-trench structures has enabled the exfoliation of materials like bismuth to sub-10
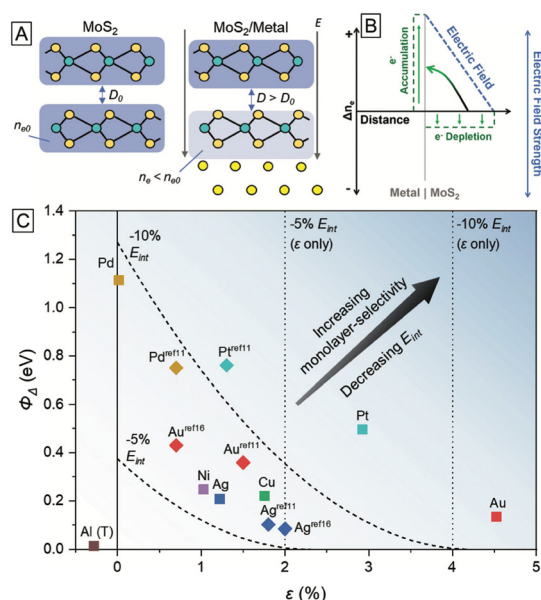
© 2025 The Author(s). Published by the Royal Society of Chemistry

RSC Appl. Interfaces, 2025, **2**, 852–872 | **859**

Fig. 4 A) Simplified schematic of the MoS$_2$/metal Schottky junction illustrating reduced interlayer energy and van der Waals (vdW) interactions. The Schottky-induced electric field distorts the electron distribution, increasing the effective interlayer distance (D) and thereby reducing vdW interactions. Electron depletion (reduced electron density n_e) leads to decreased polarisability, further diminishing vdW interactions. B) Electrostatic profile of the MoS$_2$/metal Schottky junction using the full depletion approximation. The electron density n_e (green dashed line) decreases in MoS$_2$ (right side) and correspondingly increases in the metal (left side). An electric field (blue dashed line) is established within the MoS$_2$ depletion width (x_d), peaking near the interface. The y-axis represents the change in electron density (Δn_e) or electric field strength, and the x-axis denotes the distance from the interface, with $x = 0$ at the MoS$_2$/metal interfacial plane. C) Comparison of properties of monolayer MoS$_2$/metal interfaces predicted to enable monolayer-selective MME and experimental attempts with different monolayer MoS$_2$/metal interfaces. Aluminium (Al) could not enable monolayer-selective MME, similar to other reports.[78]

nm thicknesses, which can then be analysed using atomic force microscopy and Raman spectroscopy.[75] Similarly, mechanical exfoliation has been employed to produce high-mobility layers of GdTe$_3$.[76]

One of the significant achievements with this method is the ability to produce heterostructures in a relatively easy way.[73] Additionally, this method has facilitated the analysis of electronic properties of new materials, such as one-dimensional wires and molecular wires, which are identified through photoluminescence during exfoliation.[77] As shown in Fig. 4, the mechanisms and properties of MoS$_2$/metal Schottky junctions illustrate the potential for enabling monolayer-selective mechanical modulation etching (MME).

Despite its effectiveness in producing high-quality monolayers, mechanical exfoliation is not suitable for large-scale production. The layers obtained can vary in thickness and size, and the process is labor-intensive. For instance, the process typically follows a geometric progression in thickness reduction, rather than a simple halving with each tear, which

complicates consistency.[79] Advances in automated mechanical exfoliation systems have been made to improve throughput and consistency, but these systems still struggle to meet the demands of industrial applications.[80]

To address these challenges, research has been directed towards enhancing the reproducibility and scalability of the technique. This includes developing automated systems for layer-by-layer exfoliation and transfer, as well as combining mechanical exfoliation with other techniques like CVD to produce hybrid structures with improved properties.[81]

While mechanical exfoliation remains a valuable technique for fundamental research and the production of high-quality vdW monolayers, its scalability and consistency challenges need to be addressed to meet the demands of industrial applications. Ongoing research and technological advancements are expected to enhance its practicality and expand its applications in various fields.

B. Chemical vapour deposition

Chemical vapour deposition is a widely used technique for the controlled growth of large-area vdW layers, making it crucial for practical applications. CVD involves the chemical reaction of vapour-phase precursors on a heated substrate, resulting in the deposition of thin films. This method offers precise control over the thickness, composition, and uniformity of the deposited layers, which is essential for high-quality applications.

The CVD process typically includes the following steps:

1. Precursor introduction: gaseous precursors are introduced into a reaction chamber containing the substrate. This step is critical as the choice of precursors and their flow rates determine the chemical reactions that will form the vdW layers.[82,83]

2. Reaction and deposition: the precursors decompose or react at elevated temperatures, leading to the deposition of the desired material on the substrate. For example, in the CVD growth of MoS$_2$, sulphur and molybdenum hexacarbonyl are commonly used precursors.[83]

3. Post-deposition treatments: annealing or other treatments may be applied to improve crystallinity and remove impurities. These treatments can significantly enhance the electrical and thermal properties of the deposited layers.[84,85]

CVD has been successfully employed to synthesise a variety of vdW layered materials, including graphene and transition metal dichalcogenides. This method allows the synthesis of large-area monolayers, with satisfactory results for MoS$_2$, highlighting the potential of CVD for reaching industrial level production.[83]

Additionally, CVD is suitable for the growth of complex vdW heterostructures. The layer-controlled CVD growth of MoS$_2$ vertical heterostructures *via* vdW epitaxy has shown precise control over the number of layers.[83] The development of air-stable 2D magnetic CrS$_2$ on a mica substrate using CVD is another significant advancement, offering new
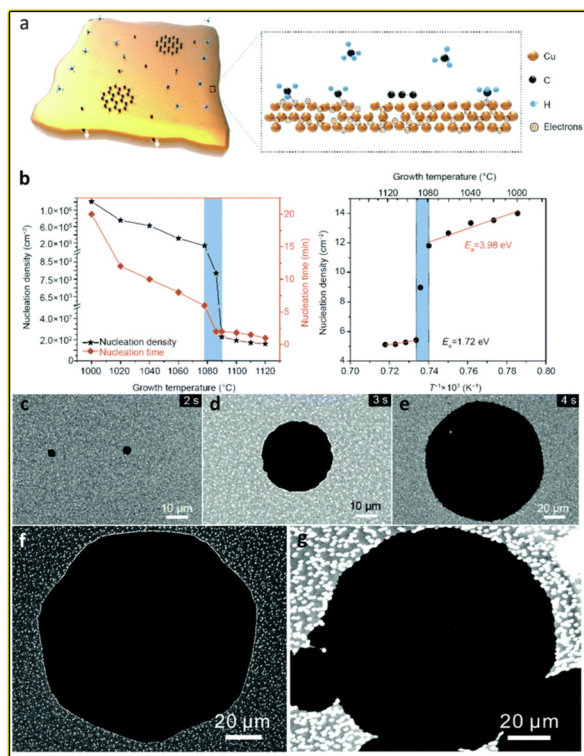
Fig. 5 a) Schematic illustration of graphene nucleation on liquid Cu under low carbon chemical potential facilitated by abundant free electrons. b) Plots of the nucleation density and nucleation time of graphene on Cu as functions of temperature. The Arrhenius plot for the nucleation density indicates the activation energies for solid and liquid Cu. c–e) Scanning electron microscopy (SEM) images showing the time evolution of graphene single crystal growth on liquid Cu at 1120 °C with 5 sccm of CH_4 for: c) $t = 2$ s, d) $t = 3$ s, and e) $t = 4$ s. Time zero ($t = 0$ s) is defined as the moment when CH_4 is introduced into the CVD furnace. f) and g) Graphene growth conducted at different precursor concentrations of CH_4: f) 5 sccm and g) 10 sccm at 1100 for 10 s.[86]

possibilities for magnetic applications at room temperature.[85] As illustrated in Fig. 5, the nucleation and growth dynamics of graphene on liquid copper (Cu) are significantly influenced by temperature and precursor concentration under low carbon chemical potential.

However, challenges remain in optimising the CVD process for different materials and ensuring scalability. Achieving uniformity over large areas, controlling the number of layers, and integrating CVD-grown materials with other processes are ongoing areas of research. For example, the anomalous thickness dependence of the Curie temperature for 1 T-CrTe$_2$ grown by CVD shows that more work is needed to understand and control these properties.[87] Furthermore, the fabrication of top-gated field-effect transistors (FETs) using CVD-grown materials highlights the need for low-temperature synthesis methods compatible with flexible substrates like glass.[88] The synthesis of GaSe/MoSe$_2$ misfit heterostructures using a two-step CVD process demonstrates the ability to create vertically stacked and lateral heterostructures with tunable electronic properties.[89]

Other important aspects are the vdW structures' surface energy and wettability, which are influenced by the underlying substrate and the dominant vdW forces, and play a crucial role in the overall performance and integration of the materials in devices.[90]

The synthesis of hexagonal boron nitride (hBN) heterostructures for 2D vdW electronics *via* CVD is another example of the method's versatility. hBN serves as an excellent insulator and is essential in constructing versatile tunnelling devices.[91] Additionally, studies on the thermal conductivity of CVD-grown Bi_2O_3Se were particularly successful.[92]

While CVD remains a cornerstone technique for high-quality synthesis, ongoing research is essential to overcome current challenges and improve scalability, uniformity, and integration. Advances in this area will continue to expand the applications of vdW materials in various fields, including electronics, photonics, and thermoelectrics.[14,16,82–85,87–96]

C. Solution-based methods

Solution-based methods, including liquid-phase exfoliation and chemical synthesis, provide an alternative approach for the large-scale production of vdW layered materials. These methods involve dispersing bulk crystals in a solvent, followed by exfoliation through sonication or chemical reactions to produce monolayers or few-layer nano-sheets.

The key steps in solution-based methods are:

1. Dispersion: bulk vdW materials are dispersed in a suitable solvent, often with the aid of surfactants to stabilise the exfoliated layers. For example, surfactants like sodium dodecyl sulphate (SDS) or organic solvents such as *N*-methyl-2-pyrrolidone (NMP) can be used to facilitate the dispersion of materials like graphene and MoS$_2$.[15]

2. Exfoliation: ultrasonication or chemical reactions are employed to exfoliate the material into individual layers or nano-sheets. Ultrasonication involves applying high-frequency sound waves to break the vdW interactions holding the layers together. This method has been effective in producing large quantities of few-layer graphene and other 2D materials.[15,17]

3. Centrifugation: the dispersion is centrifuged to separate the exfoliated layers from the unexfoliated bulk material and other impurities. Centrifugation parameters such as speed and duration are critical in achieving effective separation. High-speed centrifugation helps in isolating monolayers and few-layer nano-sheets from thicker flakes.[17]

4. Collection: the supernatant containing the exfoliated layers is collected for further processing or use. The quality of the collected material can be further enhanced through additional purification steps, such as filtering or further centrifugation.[97]

As illustrated in Fig. 6, isopycnic density gradient ultracentrifugation (iDGU) enables layer-by-layer separation of various two-dimensional materials, leading to improved thickness monodispersity. Liquid-phase exfoliation is
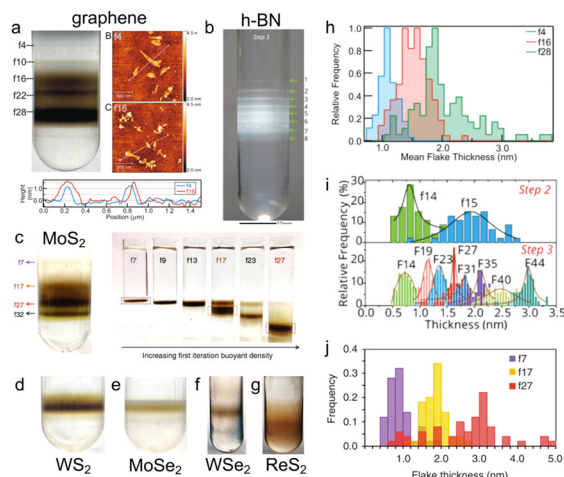
© 2025 The Author(s). Published by the Royal Society of Chemistry

RSC Appl. Interfaces, 2025, **2**, 852–872 | **861**

Fig. 6 Separation by isopycnic density gradient ultracentrifugation (iDGU). a) Layer-by-layer separation of graphene *via* iDGU. Atomic force microscopy images and cross-sectional line profiles reveal nanosheets of monolayer and bilayer thickness. b) Layer-by-layer separation of hexagonal boron nitride (h-BN) using iDGU. c–f) Layer-by-layer separation of transition metal dichalcogenides (TMDs) by iDGU with polymeric surfactants reducing the effective buoyant density: c) MoS_2, d) WS_2, e) $MoSe_2$, and f) WSe_2. g) Separation of high-density ReS_2 layers using iDGU with a mixture of iodixanol and CsCl to increase the gradient medium's buoyant density. h–j) Thickness histograms demonstrating improved monodispersity after iDGU for h) graphene, i) h-BN, and j) MoS_2.[98]

advantageous due to its simplicity, scalability, and ability to produce large quantities of material. It has been successfully used to exfoliate a wide range of vdW materials, including graphene, transition metal dichalcogenides (TMDs), and black phosphorus. For instance, black phosphorus nanosheets with high carrier mobility have been produced using liquid-phase exfoliation.[15]

Chemical synthesis approaches, such as solvothermal or hydrothermal methods, can also produce vdW materials with controlled morphology and size. These methods involve the reaction of precursors in a solvent at elevated temperatures and pressures, leading to the formation of vdW materials. Solvothermal synthesis has been used to produce MoS_2 nanosheets with precise control over size and morphology.[17] However, these methods often result in materials with defects and varying layer thicknesses, which can impact their performance. Defects such as vacancies, grain boundaries, and functional groups introduced during exfoliation can affect the electrical and thermal conductivity of the materials. Efforts to improve the quality and uniformity of solution-processed vdW materials are ongoing, with significant progress being made through the optimisation of exfoliation conditions and the development of novel solvents and stabilisers.[99] For instance, optimising the sonication power and duration can help in reducing defects and achieving a higher yield of monolayer materials. Similarly, using high-purity solvents and surfactants can minimise contamination and improve the overall quality of the exfoliated materials. The use of mixed solvents and surfactant combinations to enhance exfoliation efficiency and material quality has also been explored.[15]

While solution-based methods offer a scalable and versatile approach for producing vdW layered materials, ongoing research is essential to address the challenges related to material quality and uniformity.[15,17,97,99]

D. Challenges in scaling synthesis for industrial applications

While laboratory techniques like mechanical exfoliation and CVD provide excellent control over material properties at small scales, scaling these methods for industrial applications presents significant challenges. Mechanical exfoliation is highly effective for producing high-quality monolayers but is labor-intensive and difficult to scale for large-scale manufacturing. Conversely, CVD offers scalability but often introduces grain boundaries and non-uniformities that degrade the material's thermoelectric performance.

To address these issues, hybrid approaches are being explored, combining CVD with solution-based methods to improve scalability while maintaining high material quality. Automated mechanical exfoliation techniques and innovations in CVD growth parameters are also being developed to bridge the gap between research-grade and industrial-scale production of vdW materials. Overcoming these scaling challenges is critical for translating promising lab-scale materials into commercially viable thermoelectric devices.[100,101]

V. Characterisation and measurement of relevant thermoelectric properties

While synthesis methods control the structural and electronic properties of vdW materials, characterisation techniques provide valuable feedback to optimise synthesis protocols, understanding the materials' performance and optimising them for applications in commercial devices. They involve evaluating key parameters S, σ and κ. Advanced techniques have been developed to accurately measure these properties in low-dimensional and nano-structured materials.

For the Seebeck coefficient, micro-fabricated heater and sensor arrays allow for high-resolution measurements even in small and thin samples. The four-probe method is commonly used to measure electrical conductivity, minimising the effects of contact resistance. Thermal conductivity is measured using techniques such as the 3-omega method, time-domain thermoreflectance (TDTR), and Raman thermometry, each providing insights into the lattice and electronic contributions to thermal transport.

Hall effect measurements are essential for determining carrier concentration and mobility, which directly impact thermoelectric performance. These measurements have been refined to account for the unique properties of vdW materials, enabling accurate assessment of their potential for thermoelectric applications.

The Seebeck coefficient is typically measured using a setup where a temperature gradient is applied across a sample, and the resulting voltage difference is measured.

The Seebeck coefficient can be measured as:

$$S = -\frac{\Delta V}{\Delta T} \quad (16)$$

where ΔV is the voltage difference and ΔT is the temperature difference across the material. Accurate measurement of S requires precise control of the temperature gradient and sensitive voltage detection.

High-resolution measurements of the Seebeck coefficient in vdW materials can be achieved using micro-fabricated heater and sensor arrays. These arrays allow for localised heating and accurate measurement of the temperature gradient and voltage, even in small and thin samples such as monolayers of TMDs.[102]

Electrical conductivity is typically measured using a four-probe method to eliminate the effects of contact resistance. In the four-probe method, four electrodes are placed on the sample. A known current is passed through the outer two electrodes, and the voltage drop is measured across the inner two electrodes. The electrical conductivity is then calculated using the formula:
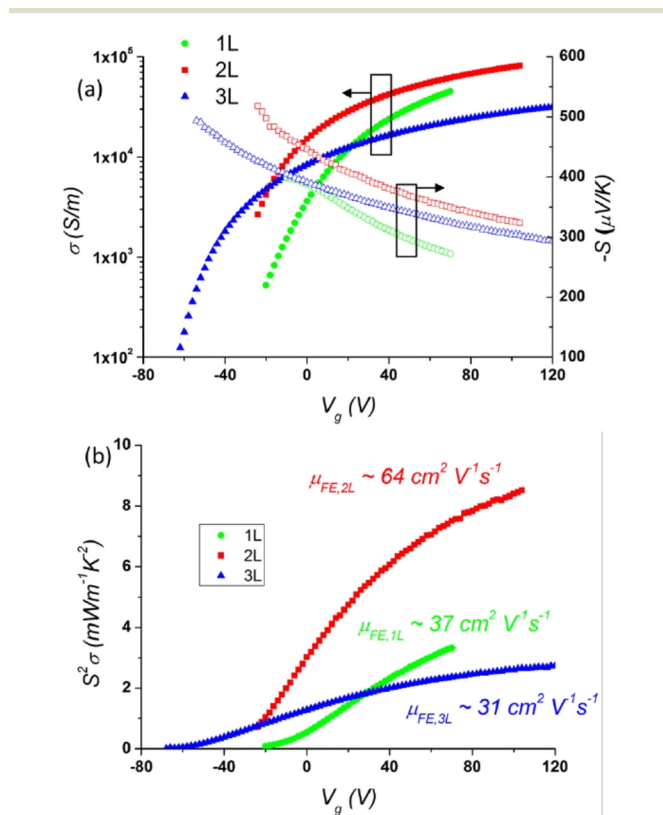
$$\sigma = \frac{I}{V} \cdot \frac{d}{A} \quad (17)$$

where I is the current, V is the voltage drop, d is the distance between the voltage probes, and A is the cross-sectional area of the sample. Fig. 7 shows a typical thermoelectric characterisation of a monolayer, done for a MoS_2 sample at room temperature. For vdW materials, especially in thin films or nano-structures, the measurement setup must account for their low-dimensional nature. This often involves micro-fabrication techniques to create well-defined geometries and precise probe placement.[103]

Thermal conductivity (κ) is typically measured using a range of options, including the 3-omega method, time-domain thermoreflectance (TDTR), and Raman thermometry.

The 3-omega method involves applying an alternating current at frequency ω through a metal heater line deposited on the sample. The resulting temperature oscillations at frequency 2ω induce a voltage response at frequency 3ω, which can be measured, as schematically illustrated in Fig. 8. The thermal conductivity is then extracted from the phase and amplitude of the 3-omega signal.[105] The method's insensitivity to both in-plane and cross-plane thermal conductivity is a limitation.

TDTR is a pump-probe technique where a short laser pulse (pump) heats the sample surface, and a time-delayed probe pulse measures the resulting temperature change by monitoring the reflectance change. The thermal conductivity is determined by analysing the heat flow dynamics in the sample.[107] However, the main limitation of this method is its scarce suitability for 2D materials. It requires a minimum sample thickness of 20 nm to measure thermal properties, leading to cross-plane heat transport, which differs significantly from in-plane transport in 2D materials due to weak interlayer coupling. For example, Jiang *et al.* found a two-order magnitude difference between in-plane and cross-plane thermal conductivities in MX_2 (M = Mo, W and X = S,

Fig. 7 Thermoelectric characterisation of monolayer MoS_2, obtained by mechanical exfoliation, at room temperature. Measurements include the Seebeck coefficient (a), electrical conductivity (a), and power factor (b) as functions of carrier concentration, where V_g is the applied gate voltage.[104]
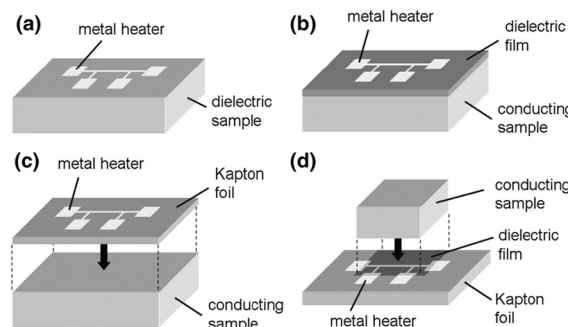

Fig. 8 Schematic illustration of the 3-omega method. a) A metal heater strip can be directly deposited on a dielectric sample. b) For electrically conductive samples, an additional dielectric layer is needed between the sample and the heater strip. c) The 3-omega sensor can be prefabricated on a standalone Kapton foil, allowing the same sensor to be used across multiple samples. d) An electrically conductive sample can also be placed on top of the prefabricated sensor if a dielectric layer is added to the heater strip.[106]

© 2025 The Author(s). Published by the Royal Society of Chemistry

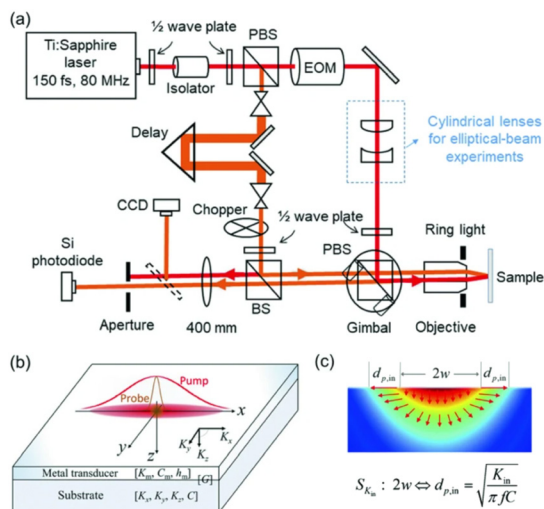*RSC Appl. Interfaces*, 2025, **2**, 852–872 | **863**

Fig. 9 a) Diagram illustrating the experimental setup for the TDTR technique. EOM, PBS, and BS represent the electro-optic modulator, polarising beam splitter, and beam splitter, respectively. b) Diagram demonstrating the elliptical-beam method applied to the sample. c) Depiction of heat flux directions and the comparison between the laser spot size and sample thickness.[108]
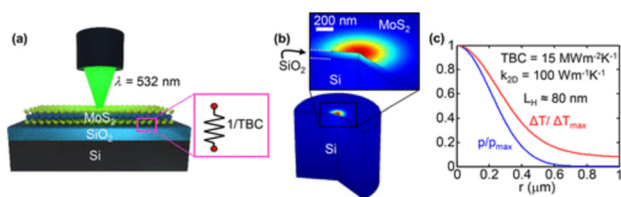

Fig. 10 Laser heating experiment and thermal model: a) schematic of the sample structure and measurement setup, highlighting the thermal boundary resistance (1/thermal boundary conductance) at the MoS_2/SiO_2 interface. b) Simulated temperature rise during laser heating using a 2D axis symmetric finite element model. c) Normalised power density and temperature rise in the MoS_2 film as a function of the radial coordinate for G = 15 MW m^{-2} K^{-1} and thermal conductivity k_{2D} = 100 W m^{-1} K^{-1}, showing a small thermal healing length ($L_H \sim$ 80 nm) compared to the laser beam size ($r_0 \sim$ 300 nm), which leads to insensitivity to the thermal conductivity of the 2D material.[110]

Se) bulk crystals.[108] Additionally, the method's costly and highly specialised setup limits its accessibility. A schematic representation is shown in Fig. 9.

Raman thermometry uses the temperature dependence of Raman peak positions to measure thermal conductivity. By analysing the shift in Raman spectra with applied heating, the thermal conductivity of the material can be inferred. This method is particularly useful for thin films and nano-structures where traditional methods may be challenging to apply.[109] The setup and measurements are illustrated in Fig. 10.

Hall effect measurements, illustrated in Fig. 11, are used to determine the carrier concentration and mobility in thermoelectric materials. In this method, a magnetic field is applied perpendicular to the current flow in the sample, and
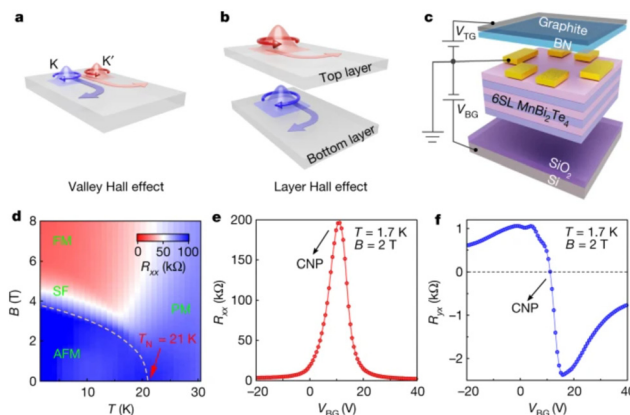

Fig. 11 Illustration of Hall effects: a) the valley Hall effect occurs in non-magnetic quantum materials like gapped graphene and transition metal dichalcogenides, where the Berry curvature is locked to the K and K′ valleys, causing electrons in opposite valleys to deflect in opposite directions. b) The layer Hall effect is observed in even-layered $MnBi_2Te_4$ in the antiferromagnetic topological insulator state, where the Berry curvature is locked to the top and bottom layers, resulting in electrons deflecting in opposite directions in these layers. c) Schematic of dual-gated devices with V_{BG} (bottom gate voltage) and V_{TG} (top gate voltage). d) Longitudinal resistance R_{xx} as a function of temperature (T) and magnetic field (B), indicating magnetic states: AFM (antiferromagnetic), FM (ferromagnetic), SF (spin-flop), and PM (permanent magnet). (e and f) R_{xx} and R_{yx} as functions of V_{BG} in the antiferromagnetic phase at B = 2 T, with CNP (charge-neutral point).[111]

the resulting Hall voltage is measured. The carrier concentration (n) and mobility (μ) can be calculated using the relations:

$$n = \frac{IB}{eV_H d} \quad (18)$$

$$\mu = \frac{\sigma}{ne} \quad (19)$$

where I is the current, B is the magnetic field, e is the electron charge, V_H is the Hall voltage, and d is the sample thickness.[23]

A precise characterisation of thermoelectric properties is required for the development and optimisation of novel vdW layered materials. Advanced measurement techniques tailored to the unique properties of these materials have significantly enhanced our understanding and ability to improve their performance.

VI. Thermoelectric 2D layered vdW materials

In this section, we discuss key 2D van der Waals materials and their measured and/or calculated thermoelectric performances, as summarised in Table 2.

Although graphene might not be an ideal thermoelectric material due to its intrinsically low Seebeck coefficient, it is the first example of a two-dimensional material and shows exceptionally high thermal conductivity, with a significant

Table 2 Summary of thermoelectric properties of various 2D materials. Single-layer (SL), multilayer (ML), and bulk-like structures are indicated, along with the experimental (Exp) or computational (DFT) data type. Values from the main studies are reported among multiple sources indicated in the main text

Material	Type	Seebeck coefficient ($\mu V\ K^{-1}$)	Power factor ($\mu W\ m^{-1}\ K^{-2}$)		Notable features
Graphene-based materials					
Graphene	SL (Exp)	~80 (p-doped)	6600 (holes), 6100 (electrons)		High thermal conductivity ($4000\ W\ m^{-1}\ K^{-1}$)
Graphene	ML (Exp)	>100	4800 (holes), 4100 (electrons)		Enhanced by heterostructures
Graphene/hBN	Heterostructure (Exp)	182	36 600 (holes), 19 000 (electrons)		Reduced scattering, higher carrier mobility
Graphene/SiO$_2$	Heterostructure (Exp)	109	—		Lower performance compared to hBN substrates
Graphene/MoS$_2$	Heterostructure (Exp)	—	High		Synergy between graphene's conductivity and MoS$_2$'s Seebeck
Phosphorene-based materials					
Black phosphorus	ML (Exp)	77–400	Up to 500		Highly anisotropic, tunable *via* thickness/doping
Exfoliated phosphorene	ML (Exp)	—	200		High power factor in thin layers (10–30 nm)
Ionic-liquid-gated phosphorene	ML (Exp)	—	500		Enhanced *via* electrostatic gating
Au-decorated phosphorene	ML (Exp)	50–400	65		Tunable *via* Au nanoparticle content
MoS$_2$ and WSe$_2$ family					
MoS$_2$	SL (Exp)	10 000	200 (single layer), 8500 (bilayer)		High carrier mobility, quantum size effects
WSe$_2$	ML (Exp)	250 (n-type), 380 (p-type)	3000		Gate-induced doping enhances performance
MoS$_2$	SL (DFT)	200	8		Predictions with spin–orbit coupling effects
MoS$_2$	SL (DFT)	—	N × 000		Band edge gradients enhance zT
MoS$_2$/WSe$_2$	Heterostructure (Exp)	10 000 (MoS$_2$), 380 (WSe$_2$)	8500		Synergistic effects enhance performance
hBN/MoS$_2$/WSe$_2$	Heterostructure (Exp)	—	—		Synergistic effects improve thermoelectric efficiency
PtSe$_2$ and PtTe$_2$ materials					
PtSe$_2$	ML (Exp)	188	—		Semi-metallic nature improves Seebeck coefficient
PtTe$_2$	ML (Exp)	—	—		Metallic behavior
Oxide-based materials					
SrTiO$_3$	Bulk (Exp)	108	0.1 (zT at 300 K)		Enhanced *via* 2D heterostructures
Nb-doped SrTiO$_3$	Bulk (Exp)	—	—		Formation of 2D electron gases enhances transport
SrTi$_{0.8}$Nb$_{0.2}$O$_3$	Bulk (Exp)	850	—		High electrical conductivity ($1.4 \times 10^3\ S\ cm^{-1}$)
TiO$_2$	ML (Exp)	124	—		Improved in TiO/SrTiO$_3$ heterostructures
TiO$_2$/SrTiO$_3$	Heterostructure (DFT)	—	—		2D electron gases improve transport properties
TiO$_2$/SrTiO$_3$	Heterostructure (Exp)	—	—		Epitaxial growth enhances mobility
SnSe-based materials					
SnSe	Bulk (Exp)	346–500	75 ($\mu W\ cm^{-1}\ K^{-2}$)		High-performance material, enhanced by doping
SnSe	ML (Exp)	—	12.5 (in-plane), 2.5 (out-of-plane)		Figure of merit (zT) reaching 1.1 at 950 K
SnSe	SL (DFT)	500	14 ($\mu W\ cm^{-1}\ K^{-2}$)		Strong anisotropy, higher in-plane conductivity
Pb-doped SnSe	Bulk (Exp)	—	75 ($\mu W\ cm^{-1}\ K^{-2}$)		Multi-band effects improve performance
Br-doped SnSe	Bulk (Exp)	—	—		Increased n-type thermoelectric efficiency
Na/Ag-doped SnSe	Bulk (Exp)	—	—		Hole doping improves thermoelectric properties
Bi$_2$Te$_3$ materials					
Bi$_2$Te$_3$	Bulk (Exp)	220	—		Optimized *via* microstructure engineering

variation of thermoelectric properties depending on its crystallinity. This makes it an ideal platform for exploring thermal transport mechanisms, tuning thermoelectric properties through structural modifications, and developing heterostructures that enhance energy conversion efficiency.

The Seebeck coefficient has been measured up to ~80 $\mu V\ K^{-1}$ in a single-crystal monolayer under p-doped conditions at room temperature, whereas in bilayer graphene the same parameter achieves a maximum value that exceeds 100 uV K^{-1} for both hole and electron carriers.[112,113] Dollfus *et al.*

© 2025 The Author(s). Published by the Royal Society of Chemistry

RSC Appl. Interfaces, 2025, **2**, 852–872 | **865**

investigated the graphene monolayer applying both ballistic Landauer transport equation and diffusive Boltzmann transport equation models, to calculate the electron and phonon transport trends.[114] They calculated the Seebeck coefficient under pristine conditions to have a relatively low value, typically below 100 μV K^{-1}, which has been attributed to its gapless nature and Dirac cones in the band structure, while its thermal conductivity is exceptionally high, around 4000 W m^{-1} K^2. In nanostructured graphene, such as graphene nanoribbons, S can be significantly increased due to quantum confinement effects that contribute to open the bandgap. For the same reason, in hydrogenated graphene (graphane), the tunable electronic properties and reduced thermal conductance can lead to larger zT.[114]

Direct measurements of black phosphorus (phosphorene) report a Seebeck coefficient ranging from 77 to 400 μV K^{-1}, reaching approximately 50 μV K^{-1} at room temperature, and it can be modulated by controlling the layer thickness and doping levels.[112] In Au-decorated phosphorene, S ranges from 50 to 400 μV K^{-1} with a power factor of 65 μW m^{-1} K^{-2}, with optimised values achieved by adjusting the content of Au nanoparticles.[112,115] In mechanically exfoliated phosphorene, the power factor reaches up to 200 μW m^{-1} K^{-2} even for thin layers (1030 nm), while ionic-liquid-gated phosphorene a power factor of 500 μW m^{-1} K^{-2} has been reported.[112] The wide range of values highlights the role of synthesis methods in controlling the material performance, where in general, mechanical exfoliation allows for precise control over layer thickness, and liquid exfoliation offers a scalable approach, although with possible introduction of undesired impurities and defects.[112,115] A computational analysis conducted by Cui *et al.* indicates how S and zT are strongly dependent on the number of layers, and that a high zT value up to 0.9 can be achieved along the armchair direction in a p-type bilayer at 500 K, which is mainly attributed to its highly anisotropic and degenerate valence band structures near the Fermi level.[116]

MoS$_2$ and WSe$_2$ are two of the most widely studied TMDCs. MoS$_2$ monolayers report a Seebeck coefficients as high as 10 mV K^{-1} at room temperature, while in WSe$_2$ it is up to 380 μV K^{-1} for p-type, and 250 μV K^{-1} for n-type carriers.[112,117] These high Seebeck coefficients are typically achieved through gate-induced doping, which increases carrier concentration while preserving high carrier mobility. The power factor for WSe$_2$ is optimised at 3000 μW m^{-1} K^{-2} for both n-type and p-type configurations, near a three-dimensional carrier density of 10^{20} cm^{-3}.[112,117] MoS$_2$, in contrast, has a measured power factor of 200 μW m^{-1} K^{-2} in single layers and up to 8500 μW m^{-1} K^{-2} for bilayer samples.[112] The ability to control layer thickness and gate-induced carriers plays a critical role in optimising these thermoelectric fundamental parameters. The synthesis by CVD allows the formation of polycrystalline films with scalable manufacturing potential, although it may introduce trade-offs in material quality compared to mechanically exfoliated monolayers, which tend to exhibit fewer defects.[112]

Electron and phonon transport properties of single layer MoS$_2$ have been analysed by Jin *et al.* using first-principles calculations within LDA approximation and Boltzmann equations.[118] Both the electronic structure and phonon dispersion relation are calculated. The sharp gradients at the edges of both conduction and valence bands and several peaks near band edges, due to the quantum size effects in the 2D structure, lead to a power factor as high as several hundreds of μW cm^{-1} K^{-2}, and are considered to be responsible for large zT values.[118] The inclusion of spin-orbit coupling in DFT calculations is crucial for making accurate predictions of transition metal dichalcogenides. The strong relativistic effects in certain transition metals can significantly influence the band structure, effective masses, and spin textures, leading to more accurate predictions of thermoelectric performance. In MoS$_2$, DFT calculations with the inclusion of SOC predict a Seebeck coefficient of 200 μV K^{-1} and a power factor of 8 μW K^{-2}.[119] Although the power factor is lower compared to other TMDCs, the relatively low lattice thermal conductivity leads to a zT value nearing 1.0 at 1000 K.[119]

Platinum dichalcogenides, such as PtSe$_2$ and PtTe$_2$, display a range of thermoelectric behaviours depending on their chalcogen elements. PtSe$_2$ behaves as a semi-metal with a Seebeck coefficient exceeding 188 μV K^{-1} at 300 K, while PtTe$_2$ demonstrates metallic behaviour.[120,121] The differences in thermoelectric performance between PtSe$_2$ and PtTe$_2$ are primarily attributed to their distinct electronic structures, where PtSe$_2$ leads to a higher Seebeck coefficient due to its semi-metallic nature. Synthesis often involves thin-film fabrication techniques for both homo- and heterostructures. Tuning the material thickness has a pronounced impact on both S and PF, indicating the flexibility of these materials in thermoelectric applications.[120,121]

Although its performance as a bulk material is limited, SrTiO$_3$ has been extensively studied for its thermoelectric potential. Indeed, SrTiO$_3$ shows a Seebeck coefficient of approximately 108 μV K^{-1}, with a low power factor and a thermoelectric figure of merit (ZT) of 0.1 at 300 K.[122] Despite these limitations, when incorporated into 2D vdW heterostructures, SrTiO$_3$ reports a significant improvement in both S and PF attributed to interface effects and the formation of two-dimensional electron gases. Synthesis of SrTiO$_3$ typically relies on pulsed laser deposition (PLD) at high temperatures in an oxygen atmosphere. This method ensures high-quality films with excellent crystallinity and minimal defects, making SrTiO$_3$ a reliable component in commercial thermoelectric devices.[122] Niobium doping in SrTiO$_3$ (SrTi$_{0.8}$Nb$_{0.2}$O$_3$) results in significant improvements of the Seebeck coefficient which reaches approximately 850 μV K^{-1} in heterostructures, with high electrical conductivity (σ = 1.4 × 10^3 S cm^{-1}).[122] The formation of high-density two-dimensional electron gases at the interface plays a pivotal role in enhancing both carrier concentration and mobility. The synthesis of niobium-doped SrTiO$_3$ *via* epitaxial growth ensures precise control over layer thickness and interface quality.

Bismuth telluride (Bi_2Te_3) is one of the most well-known thermoelectric materials, with a Seebeck coefficient of approximately 220 μV K^{-1}.[123] Its power factor can be significantly increased through microstructure optimisation, which includes techniques such as ball milling (BM) and melt spinning (MS) to reduce grain size and increase texture, leading to anisotropic increased carrier mobility.[123,124] Other methods, including mechanical alloying (MA), self-propagating synthesis (SHS), and spark plasma sintering (SPS), have been utilised to further increase Bi_2Te_3's density and electrical conductivity by promoting uniform grain growth and minimising porosity. These processes are particularly effective in exploiting the anisotropic properties of Bi_2Te_3 for thermoelectric applications.[125–127]

SnSe has emerged as a high-performance thermoelectric material, exhibiting a Seebeck coefficient from 346 to values greater than 500 μV K^{-1} at room temperature, with a strong dependence on the doping levels and carrier concentrations.[128,129] In Pb-doped SnSe, an ultrahigh power factor of approximately 75 μW cm^{-1} K^{-2} at 300 K has been achieved.[130,131] The large power factor is attributed to Pb doping, which enhances carrier concentration and introduces multi-band synergistic effects that optimise the band structure for thermoelectric performance. SnSe thermoelectric properties can be further optimised through several doping strategies, including Na or Ag substitution for hole doping, Pb doping for multi-band synglisis effects, and Bi substitution at Sn sites for n-type.[128,132] Br doping is also employed for n-type SnSe by substituting Br at Se sites.[132,133] The layered crystal is typically synthesised *via* ball milling and chemical reduction, with a two-step oxide removal process to improve material purity in final pellets.[133,134] Theoretical calculations using local density approximation and Boltzmann transport equation models predict a maximum Seebeck coefficient of 500 μV K^{-1} and a power factor of 14 μW cm^{-1} K^{-2}.[135] For doped monolayers, the in-plane power factor (12.5 μW m^{-1} K^{-2}) is significantly higher than the out-of-plane power factor (2.5 μW m^{-1} K^{-2}), attributed to differences in electrical conductivity between the two directions, with the figure of merit reaching 1.1 at 950 K.[135]

Although some 2D monolayers report a significant impact in the thermoelectric performance with respect to the 3D counterpart, the efficiency can be tuned by integrating different monolayers into carefully designed heterostructures. Interestingly, although the power factor for single-crystalline graphene is reported to be 6600 μW m^{-1} K^{-2} for holes and 6100 μW m^{-1} K^{-2} for electrons at room temperature[112,136] and bilayer graphene reports power factors of 4800 μW m^{-1} K^{-2} for holes and 4100 μW m^{-1} K^{-2} for electrons at 250 K, the same parameter reaches 36 600 μW m^{-1} K^{-2} for holes and 19 000 μW m^{-1} K^{-2} for electrons at 290 K in graphene/hBN, confirming the significant performance improvement achieved in heterostructures.[112,113,136] Similarly, the Seebeck coefficient in graphene/hBN heterostructures reaches 182 μV K^{-1} and

it results in being almost twice as large for both holes and electrons compared to graphene/SiO_2 samples (109 μV K^{-1}).[112,136] The large difference is attributed to higher carrier mobility and reduced scattering at the graphene/hBN interface compared to graphene on SiO_2. A synergistic effect between the individual layers is reported in MoS_2/WSe_2 heterostructures.[137] The Seebeck coefficient reaches up to 10 mVK^{-1} for monolayer MoS_2 and 380 μV K^{-1} for p-type WSe_2, with power factors of 8500 μW m^{-1} K^{-2}, whereas the reported value for bilayers is 3000 μW m^{-1} K^{-2}. These values were calculated within DFT using the BTE and phonon dispersion calculations. The improvement in thermoelectric performance is primarily attributed to the combination of MoS_2's high carrier mobility and WSe_2's strong Seebeck coefficient, resulting in enhanced overall thermoelectric efficiency.

In heterostructures with TiO_2, $SrTiO_3$ demonstrates improved thermoelectric performance due to the formation of two-dimensional electron gases at the interface. Bulk TiO_2 exhibits a Seebeck coefficient of 124 μV K^{-1}, but this value is significantly enhanced in TiO_2/$SrTiO_3$ heterostructures.[122] The epitaxial growth of TiO_2 on $SrTiO_3$ substrates further enhances carrier mobility, particularly along specific crystallographic directions, making these heterostructures promising candidates for high-efficiency thermoelectric devices. Measurements on graphene/MoS_2 heterostructures report a high power factor, which can be attributed to the synergy between graphene's large in-plane electrical conductivity and MoS_2's high Seebeck coefficient.[138] Additionally, hBN/graphene/hBN heterostructures show a Seebeck coefficient that is twice as large as that of graphene on SiO_2 substrates. This significant enhancement is due to the high-quality interface provided by the hBN layers, which minimises scattering and increases carrier mobility in graphene.[139]

In general, the significant zT enhancement is attributed to decreased scattering and increased carrier mobility at high-quality interfaces, which are strongly influenced by the choice of synthesis method, with mechanically exfoliated samples exhibiting fewer defects but limited scalability, while CVD enables large-scale production at the potential cost of crystal quality.[139]

VII. Considerations and future directions

Due to the high potential that engineering hetero-structures have and the vast parameter space and the combinatorial explosion of possible 2D material configurations, traditional experimental and quantum mechanics-based computational methods alone are insufficient for timely screening. Machine learning (ML) models have emerged as indispensable tools in this context, offering the ability to efficiently navigate and predict the properties of a multitude of 2D monolayers, bilayers, and more complex heterostructures.[140–143]

ML algorithms can be trained on existing datasets to identify patterns and correlations among key thermoelectric properties, such as the Seebeck coefficient, electrical conductivity, and thermal conductivity.[140,144–146] These models can rapidly predict the dimensionless figure of merit for new material combinations, thus prioritising candidates for experimental validation.

Furthermore, ML models are currently revolutionising both the synthesis and characterization of vdW materials. By analysing large datasets obtained from synthesis experiments and characterisations like Raman spectroscopy, atomic force microscopy, and electrical measurements, ML algorithms can identify patterns that guide the optimization of growth parameters and processing conditions. For example, ML models can predict the optimal CVD temperature and precursor flow rates to maximise material quality or suggest modifications to mechanical exfoliation protocols to produce defect-free layers.

In characterization, ML models can help automate the analysis of data, providing real-time feedback on material quality during the synthesis process. This allows for a more adaptive workflow, where characterization data is used to adjust synthesis techniques on the fly. This integration accelerates the discovery of high-performance thermoelectric materials by reducing the trial-and-error nature of traditional methods.

A. Challenges and future research directions

The primary advantage of using ML in this domain is the significant reduction in time and resources required to identify high-performance thermoelectric materials. Traditional approaches involve labor-intensive synthesis and characterisation processes, whereas ML models can screen thousands of materials in a fraction of the time. This is particularly crucial given the exponential increase in potential 2D heterostructures, with millions of possible bilayer combinations and trillions of trilayer configurations.[147,148]

Interface control and engineering offer vast possibilities in novel materials discovery, where by combining the properties of different materials, the resulting heterostructure will show properties that differ from the original monolayers. ML models also facilitate the discovery of non-intuitive material combinations that might be overlooked using conventional heuristic-based approaches. By leveraging large datasets and advanced algorithms, these models can uncover hidden relationships and optimise material properties beyond human intuition.[149,150]

Despite the promise of ML, several challenges remain. The accuracy of ML models heavily depends on the quality and quantity of training data. Therefore, creating comprehensive and high-quality datasets is a critical step. Moreover, the interpretability of ML models is an ongoing challenge: understanding the underlying reasons for a model's predictions is essential for gaining insights into the fundamental mechanisms governing thermoelectric properties.[151,152]

Future research need to focus on developing more sophisticated ML algorithms capable of handling the complexity and scale of vdW material combinations. This includes the integration of advanced techniques such as transfer learning, active learning, and reinforcement learning to continuously improve model performance and adapt to new data.[153,154]

Coupling ML with high-throughput computational methods can enhance the predictive power and reliability of these models. This hybrid approach can provide a robust framework for the accelerated discovery and optimisation of 2D materials for thermoelectric applications.[147,155] An example of the ML workflow is illustrated in Fig. 12, which shows how the data-driven approach leverages machine learning techniques to accelerate the discovery, design, and selection of materials by predicting their thermodynamic stability and formation energies.

The integration of machine learning in the screening of 2D materials for thermoelectric applications represents a transformative approach in materials science. By enabling efficient exploration of the vast material space, ML models can significantly accelerate the discovery and optimisation of high-performance thermoelectric materials. Addressing the challenges of data quality, model interpretability, and computational integration will be key to realising the full potential of this approach, paving the way for innovative and sustainable thermoelectric technologies.[157,158]
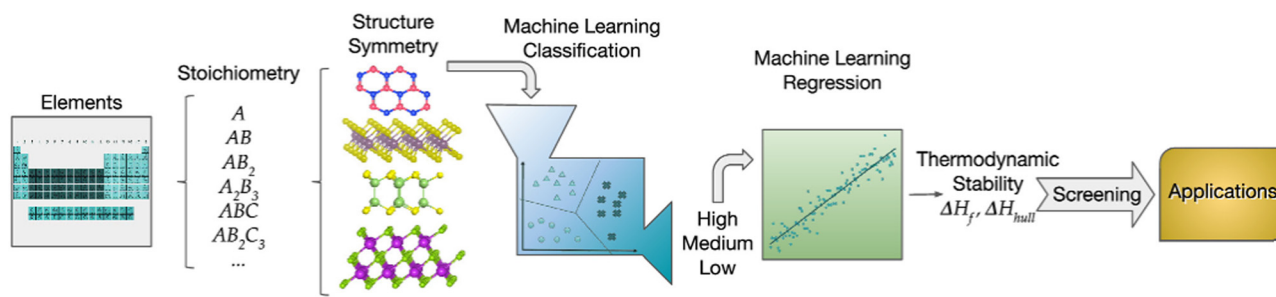

Fig. 12 Schematic illustration of a data–driven approach for materials discovery, design, and selection. From the vast number of combinations of elements, stoichiometries, and symmetries, a materials space is generated. By utilising available thermodynamic data and machine learning techniques, materials can be classified based on their thermodynamic stability. A regression model predicts formation energies, which are used to determine the convex hull of stability. Finally, stable materials are screened for potential applications.[156]

VIII. Conclusion

The exploration and development of 2 dimensional van der Waals layered materials for thermoelectric applications have revealed significant advancements, challenges, and opportunities. This review highlights the complex models that describe the thermoelectric properties, as well as the progress made in synthesising high-quality vdW materials through methods such as mechanical exfoliation, CVD, and solution-based techniques. Advantages and challenges in terms of scalability, uniformity, and result quality have been thoroughly examined, offering insights into the potential and limitations of these approaches.

The theoretical models for thermoelectric properties calculation remains a complex and challenging task due to the intricate interplay between electronic structure and phonon dynamics. The Boltzmann transport equation in the relaxation time approximation is a commonly used framework, yet it requires precise knowledge of various scattering mechanisms and relaxation times. First-principles calculations and *ab initio* molecular dynamics simulations have significantly contributed to our understanding but also highlight the need for continued advancements in computational methods.

Advanced characterisation techniques have been instrumental in accurately measuring key thermoelectric properties, including the Seebeck coefficient, electrical conductivity, and thermal conductivity. Methods such as the 3-omega technique, time-domain thermoreflectance, and Raman thermometry, along with Hall effect measurements, provide detailed insights into the electronic and thermal transport properties of these materials, and support understanding the performance of vdW materials and optimising their thermoelectric efficiency.

Despite these challenges, vdW layered materials have shown remarkable potential for thermoelectric applications. Examples of top-performing heterostructures, such as graphene/MoS_2, WSe_2/$MoSe_2$, and hBN/graphene/hBN, demonstrate the ability to achieve high thermoelectric performance through careful material design and optimisation.

Future research should focus on addressing the scalability and uniformity challenges in synthesis methods, improving the theoretical models for better prediction of thermoelectric properties, and exploring novel vdW heterostructures with enhanced performance.

Additionally, due to the large space of potential novel 2D heterostructures, integrating accurate and time-efficient machine learning models in the exploration of exotic monolayer combinations seems necessary to optimise research efforts and maximise results, therefore accelerating their widespread application in energy conversion technologies.

Data availability

No primary research results, software, or code have been included, and no new data were generated or analyzed as part of this review.

Conflicts of interest

There are no conflicts to declare.

References

1 D. M. Rowe, *Thermoelectrics Handbook: Macro to Nano*, CRC Press, 2006.
2 F. Reverter, *IEEE Sens. J.*, 2021, **21**, 22122–22132.
3 Z. Ding, G. Li, Y. Wang, C. Du, Z. Ye, L. Liang, L.-C. Tang and G. Chen, *Nano-Micro Lett.*, 2024, **16**, 242.
4 C. Chen, Z. Liu, L. Guo, B. Huo, Q. Sun, L. Liang, C. Du and G. Chen, *Adv. Funct. Mater.*, 2024, **34**, 2411490.
5 Y. Fu, H. He, T. Zhao, Y. Dai, W. Han, J. Ma, L. Xing, Y. Zhang and X. Xue, *Nano-Micro Lett.*, 2018, **10**, 1–12.
6 Q. Sun, C. Du and G. Chen, *Prog. Mater. Sci.*, 2024, 101402.
7 H. J. Goldsmid, *Introduction to Thermoelectricity*, Springer, 2010.
8 G. J. Snyder and E. S. Toberer, *Nat. Mater.*, 2008, **7**, 105–114.
9 K. S. Novoselov, A. Mishchenko, A. Carvalho and A. Castro Neto, *Science*, 2016, **353**, aac9439.
10 A. K. Geim and K. S. Novoselov, *Nat. Mater.*, 2007, **6**, 183–191.
11 A. A. Balandin, *Nat. Mater.*, 2011, **10**, 569–581.
12 M. Chhowalla, H. J. Shin, G. Eda, L.-J. Li, K. P. Loh and H. Zhang, *Nat. Chem.*, 2013, **5**, 263–275.
13 A. J. Mannix, Z. Zhang, N. P. Guisinger, B. I. Yakobson and M. C. Hersam, *Nat. Nanotechnol.*, 2017, **12**, 450–460.
14 X. Li, W. Cai, J. An, S. Kim, J. Nah, D. Yang, R. Piner, A. Velamakanni, I. Jung and E. Tutuc, *et al.*, *Science*, 2009, **324**, 1312–1314.
15 J. N. Coleman, *et al.*, *Science*, 2011, **331**, 568–571.
16 Y. H. Lee, *et al.*, *Adv. Mater.*, 2012, **24**, 2320–2325.
17 Y. Sun, *et al.*, *J. Am. Chem. Soc.*, 2012, **134**, 20244–20247.
18 G. Chen, M. S. Dresselhaus, G. Dresselhaus, J. P. Fleurial and T. Caillat, *Int. Mater. Rev.*, 2003, **48**, 45–66.
19 Y. Xu, *et al.*, *Nature*, 2014, **516**, 678–681.
20 Q. Zhang, *et al.*, *Adv. Mater.*, 2014, **26**, 4828–4875.
21 Y. Sun, Y. Zhou, J. Han, W. Liu, C. Nan, Y. Lin, M. Hu and B. Xu, *npj Comput. Mater.*, 2019, **5**, 97.
22 Y. Zhou and L.-D. Zhao, *Adv. Mater.*, 2017, **29**, 1702676.
23 K. Novoselov, A. Geim, S. Morozov, D. Jiang, Y. Zhang, S. Dubonos, I. Grigorieva and A. Firsov, *Science*, 2004, **306**, 666–669.
24 M. A. Asl, M. R. Benam, R. P. Shahri, A. Feyzi and F. Kafi, *Micro Nanostruct.*, 2022, **163**, 107134.
25 S. Li, C. Xin, X. Liu, Y. Feng, Y. Liu, J. Zheng, F. Liu, Q. Huang, Y. Qiu and J. He, *et al.*, *Nano Energy*, 2016, **30**, 780–789.

26 X. Gu, Y. Wei, X. Yin, B. Li and R. Yang, *Rev. Mod. Phys.*, 2018, **90**, 041002.

27 Q. Hao, Y. Xiao and S. Wang, *Int. J. Heat Mass Transfer*, 2020, **153**, 119636.

28 A. A. Balandin, *Nat. Mater.*, 2011, **10**, 569–581.

29 G. Chen, *Nanoscale Energy Transport and Conversion: A Parallel Treatment of Electrons, Molecules, Phonons, and Photons*, Oxford University Press, 2005.

30 X.-K. Chen, Y.-J. Zeng and K.-Q. Chen, *Front. Mater.*, 2020, **7**, 578791.

31 R. Gupta, N. Kumar, P. Kaur and C. Bera, *Phys. Chem. Chem. Phys.*, 2020, **22**, 18989–19008.

32 P. Gorai, V. Stevanović and E. S. Toberer, *Nat. Rev. Mater.*, 2017, **2**, 1–16.

33 M. A. Iqbal, N. Ashraf, W. Shahid, D. Afzal, F. Idrees and R. Ahmad, *Density Functional Theory-Recent Advances, New Perspectives and Applications*, 2021.

34 A. A. C. Alvarez, M. Bibes, W. Prellier and J. Varignon, *Phys. Rev. B*, 2023, **107**, 115109.

35 J. P. Perdew, K. Burke and M. Ernzerhof, *Phys. Rev. Lett.*, 2008, **77**, 3865–3868.

36 J. Sun, A. Ruzsinszky and J. P. Perdew, *Phys. Rev. Lett.*, 2015, **115**, 036402.

37 J. Heyd, G. E. Scuseria and M. Ernzerhof, *J. Chem. Phys.*, 2003, **118**, 8207–8215.

38 K. Berland, V. R. Cooper, K. Lee, E. Schröder, T. Thonhauser, P. Hyldgaard and B. I. Lundqvist, *Rep. Prog. Phys.*, 2015, **78**, 066501.

39 J. Klime and A. Michaelides, *J. Chem. Phys.*, 2012, **137**, 120901.

40 G. Romn-Prez and J. M. Soler, *Phys. Rev. Lett.*, 2009, **103**, 096102.

41 A. Cantarero and F. X. Àlvarez, *Nanoscale Thermoelectrics*, 2014, pp. 1–39.

42 G. K. Madsen and D. J. Singh, *Comput. Phys. Commun.*, 2006, **175**, 67–71.

43 A. J. H. McGaughey and M. Kaviany, *Phys. Rev. B: Condens. Matter Mater. Phys.*, 2004, **69**, 094303.

44 A. Ward and D. Broido, *Phys. Rev. B: Condens. Matter Mater. Phys.*, 2010, **81**, 085205.

45 S. A. Christenson, *et al.*, *Phys. Rev. B*, 2018, **97**, 045201.

46 D. G. Cahill, P. V. Braun, G. Chen, D. R. Clarke, S. Fan, K. E. Goodson, P. Keblinski, W. P. King, G. D. Mahan and A. Majumdar, *et al.*, *Appl. Phys. Rev.*, 2014, **1**, 1.

47 Y. Kikuchi, K. Tsumura and T. Kunihiro, *arXiv*, 2016, preprint, arXiv:1604.07458, DOI: 10.48550/arXiv.1604.07458.

48 S. Cha and S.-M. Hong, *Proceedings of the International Conference on Simulation of Semiconductor Processes and Devices (SISPAD)*, 2018, pp. 145–148.

49 U. Lei and N. Horing, *Phys. Rev. B: Condens. Matter Mater. Phys.*, 1987, **35**, 6281.

50 M. Galler and F. Schürrer, *AIP Conference Proceedings*, 2005, pp. 64–69.

51 D. K. Ferry and S. M. Goodnick, *Transport in Nanostructures*, Cambridge University Press, Cambridge, UK, 1997.

52 N. W. Ashcroft and N. D. Mermin, *Solid State Physics*, Holt, Rinehart and Winston, New York, 1976.

53 H. Smith and H. H. Jensen, *Transport Phenomena*, Oxford University Press, Oxford, UK, 1989.

54 S. Ahmad, F. Khan, B. Amin and I. Ahmad, *J. Solid State Chem.*, 2021, **299**, 122189.

55 R. Landauer, *IBM J. Res. Dev.*, 1957, **1**, 223–231.

56 R. Landauer, *Philos. Mag.*, 1970, **21**, 863–867.

57 S. Datta, *Quantum Transport: Atom to Transistor*, Cambridge University Press, Cambridge, 2005.

58 S. Datta, *Electronic Transport in Mesoscopic Systems*, Cambridge University Press, Cambridge, 1995.

59 M. Büttiker, *Phys. Rev. B: Condens. Matter Mater. Phys.*, 1988, **38**, 9375–9389.

60 H. L. Engquist and P. W. Anderson, *Phys. Rev. B: Condens. Matter Mater. Phys.*, 1981, **24**, 1151–1154.

61 G. Özbal, R. T. Senger, C. Sevik and H. Sevinçli, *Phys. Rev. B*, 2019, **100**, 085415.

62 Y. Imry, *Introduction to Mesoscopic Physics*, Oxford University Press, New York, 1997.

63 S. Melkonyan, T. A. Zalinyan and S. S. Melkonyan, *J. Comput. Electron.*, 2018, **17**, 328.

64 P. Allu and S. Mazumder, *Int. J. Heat Mass Transfer*, 2016, **101**, 764–771.

65 R. Gebauer and R. Car, *Phys. Rev. B: Condens. Matter Mater. Phys.*, 2003, **70**, 125324.

66 K. T. Regner, J. P. Freedman and J. A. Malen, *Nanoscale Microscale Thermophys. Eng.*, 2015, **19**, 183–205.

67 A. Togo, *J. Phys. Soc. Jpn.*, 2023, **92**, 012001.

68 Y. Quan, S. Yue and B. Liao, *Nanoscale Microscale Thermophys. Eng.*, 2021, **25**, 73–90.

69 S.-Y. Yue, R. Yang and B. Liao, *Phys. Rev. B*, 2019, **100**, 115408.

70 M. Lax and W. Cai, *Int. J. Mod. Phys. B*, 1992, **6**, 1863.

71 G. Zeng, *J. Nanosci. Nanotechnol.*, 2001, **1**, 285.

72 M. Velický, P. Tóth, A. M. Rakowski, A. P. Rooney, A. Kozikov, C. R. Woods, A. Mishchenko, L. Fumagalli, J. Yin and V. Zólyomi, *et al.*, *Nat. Commun.*, 2016, **8**, 14410.

73 T. Machida, R. Moriya, M. Aral, Y. Sata, T. Yamaguchi, N. Yabuki, S. Morikawa, S. Masubuchi and K. Ueno, *2015 IEEE International Electron Devices Meeting (IEDM)*, 2015, pp. 8–9.

74 M. Onodera, S. Masubuchi, R. Moriya and T. Machida, *Jpn. J. Appl. Phys.*, 2020, **59**, SI0802.

75 O. Yu, R. Allgayer, S. Godin, J. Lalande, P. Fossati, C. Hsu, T. Szkopek and G. Gervais, *APL Mater.*, 2023, **11**, 011102.

76 S. Lei, J.-J. Lin, Y. Jia, M. J. Gray, A. Topp, G. Farahi, S. Klemenz, T. Gao, F. Rodolakis and J. L. McChesney, *et al.*, *Sci. Adv.*, 2019, **6**, eaay6407.

77 Y. Zhu, D. Rehn, E. R. Antoniuk, G. Cheon, R. Freitas, A. Krishnapriyan and E. J. Reed, *ACS Nano*, 2021, **15**, 8779–8786.

78 A. Corletto, M. Fronzi, A. K. Joannidis, P. C. Sherrell, M. J. Ford, D. A. Winkler, J. G. Shapter, J. Bullock and A. V. Ellis, *Adv. Mater. Interfaces*, 2024, **11**, 2300686.

79 M. Tamulewicz-Szwajkowska, S. Zelewski, J. Seraficzuk and R. Kudrawiec, *AIP Adv.*, 2022, **12**, 025005.

80 H. Yang, F. Wang, H. Zhang, L. Guo, L. Hu, L. Wang, D. Xue and X. Xu, *J. Am. Chem. Soc.*, 2020, **142**, 2490–2495.

81 S.-O. Yoon, J. Jeon, K. H. Choi, B.-J. Jeong, S. Chae, B. J. Kim, S.-L. Oh, C. Woo, B.-Y. Lee and S.-H. Cho, *et al.*, *ACS Appl. Mater. Interfaces*, 2021, **13**, 60555–60563.

82 H.-Q. Qi, L. Wang, J. Sun, Y. Long, P. Hu, F. Liu and X. He, *Crystals*, 2018, **8**, 35.

83 L. Samad, S. M. Bladow, Q. Ding, J. Zhuo, R. M. Jacobberger, M. S. Arnold and S. Jin, *ACS Nano*, 2016, **10**, 7039–7046.

84 X. Zhou, X. Hu, J. Yu, S.-Y. Liu, Z. Shu, Q. Zhang, H. Li, Y. Ma, H. Xu and T. Zhai, *Adv. Funct. Mater.*, 2018, **28**, 1706587.

85 H. Xiao, W. Zhuang, L. Loh, T. Liang, A. Gayen, P. D. Ye, M. Bosman, G. Eda, X. Wang and M. Xu, *Adv. Mater. Interfaces*, 2022, **9**, 2201353.

86 Z. Kang, Z. Zheng, H. Wei, Z. Zhang, X. Tan, L. Xiong, T. Zhai and Y. Gao, *Sensors*, 2019, **19**, 1099.

87 L. Meng, Z. Zhou, M. Xu, S. Yang, K. Si, L. Liu, X. Wang, H. Jiang, B. Li and P. Qin, *et al.*, *Nat. Commun.*, 2021, **12**, 117.

88 J. R. Nasr, *PhD Thesis*, Pennsylvania State University, 2022.

89 X. Li, M.-W. Lin, J. Lin, B. Huang, A. A. Puretzky, C. Ma, K. Wang, W. Zhou, S. T. Pantelides and M. Chi, *et al.*, *Sci. Adv.*, 2016, **2**, e1501882.

90 M. Annamalai, K. Gopinadhan, S. A. Han, S. Saha, H. Park, E. B. Cho, B. Kumar, A. Patra, S.-W. Kim and T. Venkatesan, *Nanoscale*, 2015, **7**, 5440–5446.

91 K. K. Kim, H. Y. Lee and Y. H. Lee, *Chem. Soc. Rev.*, 2018, **47**, 6342–6369.

92 M. T. Hossain and P. K. Giri, *Appl. Phys. Lett.*, 2021, **118**, 163101.

93 G. Han, D. L. Duong, D. H. Keum, S.-M. Yun and Y. H. Lee, *Chem. Rev.*, 2018, **118**, 6297–6336.

94 G. Noh, H. Song, H.-S. Choi, M. Kim, J. H. Jeong, Y. Lee, M. Kim, S. Oh, M.-K. Jo and D.-H. Woo, *et al.*, *Adv. Mater.*, 2022, **34**, 2204982.

95 R. Ai, X. Guan, J. Li, K. Yao, P. Chen, Z. Zhang, X. Duan and X. Duan, *ACS Nano*, 2017, **11**, 4491–4500.

96 M. J. Moody, J. T. Paul, P. J. M. Smeets, R. d. Reis, J.-S. Kim, C. Mead, J. T. Gish, M. C. Hersam, M. K. Y. Chan and L. J. Lauhon, *ACS Appl. Mater. Interfaces*, 2023, **15**, 54091–54101.

97 L. R. L. Goncalves, J. G. Rocha, C. Couto, P. Alpuim, G. Min, D. M. Rowe and J. H. Correia, *J. Micromech. Microeng.*, 2007, **17**, S168.

98 J. Kang, V. K. Sangwan, J. D. Wood and M. C. Hersam, *Acc. Chem. Res.*, 2017, **50**, 943–951.

99 M. P. Vallin and R. Z. Zhang, *ASME 2020 International Mechanical Engineering Congress and Exposition*, 2020, p. V010T10A051.

100 A. Hoang, Q. Le and N. Vu, *Nanoscale*, 2021, **13**, 5004–5012.

101 M. Xu, Y. Li, Z. Zhou and J. Liu, *MRS Bull.*, 2020, **45**, 408–416.

102 E. Pop, *J. Appl. Phys.*, 2016, **119**, 082502.

103 K. Novoselov, A. Geim, S. Morozov, D. Jiang, M. Katsnelson, I. Grigorieva, S. Dubonos and A. Firsov, *Nature*, 2005, **438**, 197–200.

104 X. Ke, Fabrication and characterization of van der Waals heterostructure thermoelectric devices, *Master's thesis*, University of Manchester, 2021, DOI: **10.48550/arXiv.1505.06779**.

105 D. G. Cahill, M. Katiyar and J. Abelson, *Rev. Sci. Instrum.*, 1990, **61**, 802–808.

106 O. Hahtela, M. Ruoho, E. Mykkänen, K. Ojasalo, J. Nissilä, A. Manninen and M. Heinonen, *Int. J. Thermophys.*, 2015, **36**, 3255–3271.

107 D. G. Cahill, W. Ford, K. Goodson, G. Mahan, A. Majumdar, H. J. Maris, R. Merlin and S. Phillpot, *Rev. Sci. Instrum.*, 2004, **75**, 5119–5122.

108 P. Jiang, X. Qian and R. Yang, *Rev. Sci. Instrum.*, 2018, **89**, 094902.

109 A. A. Balandin, S. Ghosh, W. Bao, I. Calizo, D. Teweldebrhan, F. Miao and C. N. Lau, *Nano Lett.*, 2008, **8**, 902–907.

110 E. Yalon, B. Aslan, K. K. Smithe, C. J. McClellan, S. V. Suryavanshi, F. Xiong, A. Sood, C. M. Neumann, X. Xu and K. E. Goodson, *et al.*, *ACS Appl. Mater. Interfaces*, 2017, **9**, 43013–43020.

111 A. Gao, Y.-F. Liu, C. Hu, J.-X. Qiu, C. Tzschaschel, B. Ghosh, S.-C. Ho, D. Bérubé, R. Chen and H. Sun, *et al.*, *Nature*, 2021, **595**, 521–525.

112 K. Kanahashi, J. Pu and T. Takenobu, *Adv. Energy Mater.*, 2020, **10**, 1902842.

113 J. Briones-Torres, R. Pérez-Álvarez, S. Molina-Valdovinos and I. Rodríguez-Vargas, *Sci. Rep.*, 2021, **11**, 13872.

114 P. Dollfus, V. H. Nguyen and J. Saint-Martin, *J. Phys.: Condens. Matter*, 2015, **27**, 133204.

115 S. Lin, Y. Chui, Y. Li and S. P. Lau, *FlatChem*, 2017, **2**, 15–37.

116 Y.-F. Cui, S. Duan, X. Chen, M.-M. Yang, B.-C. Yang, W.-C. Yi and X.-B. Liu, *Vacuum*, 2021, **183**, 109790.

117 M. Yoshida, T. Iizuka, Y. Saito, M. Onga, R. Suzuki, Y. Zhang, Y. Iwasa and S. Shimizu, *Nano Lett.*, 2016, **16**, 2061–2065.

118 Z. Jin, Q. Liao, H. Fang, Z. Liu, W. Liu, Z. Ding, T. Luo and N. Yang, *Sci. Rep.*, 2015, **5**, 18342.

119 D. P. Rai, T. V. Vu, A. Laref, M. A. Hossain, E. Haque, S. Ahmad, R. Khenata and R. K. Thapa, *RSC Adv.*, 2020, **10**, 1–12.

120 W.-Y. Lee, M.-S. Kang, G.-S. Kim, J. W. Choi, N.-W. Park, Y. Sim, Y.-H. Kim, M.-J. Seong, Y.-G. Yoon and E. Saitoh, *et al.*, *ACS Nano*, 2022, **16**, 3404–3416.

121 W.-Y. Lee, M.-S. Kang, J. W. Choi, S.-H. Kim, N.-W. Park, G.-S. Kim, Y.-H. Kim, E. Saitoh, Y.-G. Yoon and S.-K. Lee, *Adv. Sci.*, 2022, **9**, 2203455.

122 H. Ohta, S.-W. Kim, Y. Mune, T. Mizoguchi, K. Nomura, S. Ohta, T. Nomura, Y. Nakanishi, Y. Ikuhara and M. Hirano, *et al.*, *Nat. Mater.*, 2007, **6**, 129–134.

123 S.-I. Kim, K.-H. Lee, H.-A. Mun, H.-S. Kim, S.-W. Hwang, J.-W. Roh, D.-J. Yang, W.-H. Shin, X.-S. Li, Y.-H. Lee, G. J. Snyder and S.-W. Kim, *Science*, 2015, **348**, 109–114.

124 B. Poudel, Q. Hao, Y. Ma, Y. Lan, A. Minnich, B. Yu, X. Yan, W. Xie, D. Wang, A. Muto, D. Vashaee, X. Chen, J. Liu, M. S. Dresselhaus, G. Chen and Z. Ren, *Science*, 2008, **320**, 634–638.

© 2025 The Author(s). Published by the Royal Society of Chemistry

RSC Appl. Interfaces, 2025, **2**, 852–872 | 871

125 F. Hao, T. Xing, P. Qiu, P. Hu, T. Wei, D. Ren, X. Shi and L. Chen, *ACS Appl. Mater. Interfaces*, 2018, **10**, 21372–21379.

126 G. Zheng, X. Su, T. Liang, Q. Lu, Y. Yan, C. Uher and X. Tang, *J. Mater. Chem. A*, 2015, **3**, 6603–6610.

127 W. Xie, J. He, H. Kang, X. Tang, T. Zhu, M. Laver, S. Wang, J. R. D. Copley, C. M. Brown, Q. Zhang and T. M. Tritt, *Nano Lett.*, 2010, **10**, 3283–3289.

128 L. Zhao, S.-H. Lo, Y. Zhang, H. Sun, G. Tan, C. Uher, C. Wolverton, V. P. Dravid and M. G. Kanatzidis, *Nature*, 2014, **508**, 373–377.

129 X.-L. Shi, X. Tao, J. Zou and Z.-G. Chen, *Adv. Sci.*, 2020, **7**, 1902923.

130 L. Zhao, G. Tan, S. Hao, J. He, Y. Pei, H. Chi, H. Wang, S. Gong, H. Xu, V. P. Dravid, C. Uher, G. J. Snyder, C. Wolverton and M. G. Kanatzidis, *Science*, 2016, **351**, 141–144.

131 K. Peng, X. Lu, H. Zhan, S. Hui, X. Tang, G. Wang, J. Dai, C. Uher, G. Wang and X. Zhou, *Energy Environ. Sci.*, 2016, **9**, 454–460.

132 A. T. Duong, V. Q. Nguyen, G. Duvjir, V. T. Duong, S. Kwon, J. Y. Song, J. K. Lee, J. E. Lee, S. Park, T. H. Min, J. Lee, J. Kim and S. Cho, *Nat. Commun.*, 2016, **7**, 13713.

133 A. Banik and K. Biswas, *Joule*, 2019, **3**, 631–640.

134 Y. Lee, Z.-Z. Luo, S.-P. Cho, M. G. Kanatzidis and I. Chung, *Joule*, 2019, **3**, 719–733.

135 S. S. Das, M. G. Rosul and M. Zebarjadi, *J. Appl. Phys.*, 2021, **129**, 1–12.

136 J. Duan, X. Wang, X. Lai, G. Li, K. Watanabe, T. Taniguchi, M. Zebarjadi and E. Y. Andrei, *Proc. Natl. Acad. Sci. U. S. A.*, 2016, **113**, 14272–14276.

137 W. Huang, X. Luo, C. K. Gan, S. Y. Quek and G. Liang, *Phys. Chem. Chem. Phys.*, 2014, **16**, 10866–10874.

138 S. Kim, C. Lee, Y. S. Lim and J.-H. Shim, *ACS Omega*, 2020, **6**, 278–283.

139 S. W. Makumi, D. Bem, N. Musila, C. Foss and Z. Aksamija, *J. Phys.: Condens. Matter*, 2023, **35**, 155701.

140 B. Mortazavi, E. V. Podryabinkin, I. S. Novikov, T. Rabczuk, X. Zhuang and A. V. Shapeev, *Comput. Phys. Commun.*, 2021, **258**, 107583.

141 E. D. Cubuk, *et al.*, *Sci. Adv.*, 2019, **5**, eaaw5841.

142 M. Fronzi, S. A. Tawfik, M. A. Ghazaleh, O. Isayev, D. A. Winkler, J. Shapter and M. J. Ford, *Adv. Theory Simul.*, 2020, **3**, 2000029.

143 M. Fronzi, O. Isayev, D. A. Winkler, J. G. Shapter, A. V. Ellis, P. C. Sherrell, N. A. Shepelin, A. Corletto and M. J. Ford, *Adv. Intell. Syst.*, 2021, **3**, 2100080.

144 Q. Yang, *et al.*, *Wiley Interdiscip. Rev.: Comput. Mol. Sci.*, 2020, **10**, e1448.

145 Z. Hou, Y. Takagiwa, Y. Shinohara, Y. Xu and K. Tsuda, *ACS Appl. Mater. Interfaces*, 2019, **11**, 11545–11554.

146 Y. Gan, G. Wang, J. Zhou and Z. Sun, *npj Comput. Mater.*, 2021, **7**, 176.

147 S. S. Chong, Y. S. Ng, H.-Q. Wang and J.-C. Zheng, *Front. Phys.*, 2024, **19**, 13501.

148 E. Yildirim and Ö. C. Yelgel, in *New Materials and Devices for Thermoelectric Power Generation*, IntechOpen, 2023.

149 M. Reis, F. Gusev, N. G. Taylor, S. H. Chung, M. D. Verber, Y. Z. Lee, O. Isayev and F. A. Leibfarth, *J. Am. Chem. Soc.*, 2021, **143**, 17677–17689.

150 S. Kadulkar, Z. M. Sherman, V. Ganesan and T. M. Truskett, *Annu. Rev. Chem. Biomol. Eng.*, 2022, **13**, 235–254.

151 J. F. Rodrigues Jr, L. Florea, M. C. F. de Oliveira, D. Diamond and O. N. Oliveira Jr, *Discover Mater.*, 2021, **1**, 1–12.

152 X. Zhong, B. Gallagher, S. Liu, B. Kailkhura, A. Hiszpanski and T. Y.-J. Han, *npj Comput. Mater.*, 2022, **8**, 1–12.

153 K. Choudhary, K. F. Garrity, S. T. Hartman, G. Pilania and F. Tavazza, *Phys. Rev. Mater.*, 2023, **7**, 1–12.

154 Z. Zhu, K. Lin, A. K. Jain and J. Zhou, *IEEE Transactions on Pattern Analysis and Machine Intelligence*, 2023, **45**, 13344–13362.

155 R. K. Vasudevan, K. Choudhary, A. Mehta, R. Smith, G. Kusne, F. Tavazza, L. Vlcek, M. Ziatdinov, S. V. Kalinin and J. Hattrick-Simpers, *MRS Commun.*, 2019, **9**(3), 821–838.

156 G. R. Schleder, C. M. Acosta and A. Fazzio, *ACS Appl. Mater. Interfaces*, 2019, **12**(18), 20149–20157.

157 S. Sarikurt, T. Kocaba and C. Sevik, *J. Mater. Chem. A*, 2020, **8**, 1–12.

158 D. Li, Y. Gong, Y. Chen, J. Lin, Q. Khan, Y. Zhang, Y. Li, H. Zhang and H. Xie, *Nano-Micro Lett.*, 2020, **12**, 1–12.